PAPER

Severe haemodynamic stress in selected subtypes of patients with moyamoya disease: a positron emission tomography study

T Nariai, Y Matsushima, S Imae, Y Tanaka, K Ishii, M Senda, K Ohno

J Neurol Neurosurg Psychiatry 2005;**76**:663–669. doi: 10.1136/jnnp.2003.025049

See end of article for authors' affiliations

Correspondence to: Dr Tadashi Nariai, Department of Neurosurgery, Tokyo Medical and Dental University, 1-5-45 Yushima, Bunkyo-ku, Tokyo 113-8519 Japan; nariai.nsrg@tmd.ac.jp

Received 31 July 2003
In revised form
7 September 2004
Accepted
7 September 2004

Background: The optimum management of patients with moyamoya disease remains controversial.
Objectives: To examine retrospectively the correlation between the degree of haemodynamic stress and the clinical presentation by measuring cerebral haemodynamics and metabolism using positron emission tomography (PET).
Methods: 57 patients with moyamoya disease (mean age 32 years, range 12 to 64), classified into five groups according to clinical manifestations, underwent PET measurement of cerebral blood flow (CBF), cerebral blood volume (CBV), cerebral metabolic rate for oxygen ($CMRO_2$), and oxygen extraction fraction (OEF) using ^{15}O labelled gases. The regional values in patient groups were compared with a normal group.
Results: CBF in non-symptomatic patients, patients presenting with transient ischaemic attacks (TIA), and patients with haemorrhagic onset (H) was not significantly lower than in normal controls in any region. CBV in the TIA group and in patients with infarction associated with TIA (I/TIA) was significantly higher than in the controls in most regions. OEF in the frontal, parietal, and temporal cortex was significantly higher in the I/TIA group than in the controls. Patients in the H group and those with a permanent deficit with infarction (PD group) had decreased metabolism with normal OEF. Multivariate analysis to test the distribution of the three dimensional vector (CBF, CBV, OEF) showed significant differences between every possible pair among the six groups except NS v H and H v PD in the frontal cortex.
Conclusions: The haemodynamic status of moyamoya disease is not uniform, and severe haemodynamic stress occurs in selected subgroups of patients.

Moyamoya disease is characterised as a progressive occlusion of the terminal portion of the bilateral internal carotid artery, accompanied by the development of collateral networks to compensate for the reduced cerebral perfusion.[1] Although these features are common to all patients with the syndrome, the clinical presentation is not uniform. Ischaemic symptoms are the most frequent clinical feature in the juvenile population, but the severity of the ischaemia is variable. Some patients have only transient motor deficit with well preserved intelligence, while others present with progressive stroke and severe mental retardation or persistent neurological deficits. Haemorrhagic events are more common in the adult than in the juvenile population, although ischaemic presentation in adults is by no means uncommon.[2–4] In recent years, we have also encountered non-symptomatic cases incidentally diagnosed by magnetic resonance (MR) angiography. This variability in the clinical presentation of moyamoya disease might reflect a variable interaction between the worsening haemodynamics with disease progression and the protection conferred by collateral development. We postulated that the degree of haemodynamic compromise may vary in patients with different clinical manifestations.

Although there have been many reports on the preoperative haemodynamic pattern and its improvement with surgical treatment,[5–9] there is still controversy over the management of this disease.[10 11] This may arise partly because patients were treated without clarifying their variable haemodynamic factors. It is our assumption that the optimum treatment strategy for each clinical presentation should be determined by knowledge of the particular haemodynamic conditions.

In the present study, we retrospectively analysed the cerebral haemodynamics and metabolism data in 57 Japanese patients with moyamoya disease, mainly adults, obtained using positron emission tomography (PET) between 1991 and 2000. We attempted to clarify the correlation between the clinical presentation and the haemodynamic findings in order to determine the optimal treatment strategy for each disease subtype.

METHODS

Subjects

The study subjects included 57 consecutive patients with moyamoya disease aged over 10 years (mean age 32 years, range 12 to 64). We divided them into five groups based on the clinical presentation.

Non-symptomatic patients

Seven patients were non-symptomatic (NS group; mean age 28 years, range 17 to 40); they were free of focal ischaemic symptoms but had been incidentally diagnosed on magnetic resonance imaging (MRI) and MR angiography. The reason for MRI screening was either that they had a relative with the disease or that they had non-ischaemic symptoms such as chronic headache. None of these subjects had infarcted lesions on MRI.

Abbreviations: CBF, cerebral blood flow; CBV, cerebral blood volume; $CMRO_2$, cerebral metabolic rate for oxygen; MTT, mean transit time; OEF, oxygen extraction fraction; PET, positron emission tomography; ROI, region of interest; TIA, transient ischaemic attack

Table 1 Regional data for frontal, parietal, and temporal cortices

	Lower frontal	Upper frontal	Sensorimotor	Parietal	Temporal
CBF (ml/min/100 g)					
Normal (n = 6)	42.8 (10.0)	41.8 (10.2)	40.9 (11.2)	40.7 (8.9)	44.4 (13.2)
NS (n = 7)	45.6 (7.7)	44.8 (8.1)	43.1 (8.5)	43.6 (6.5)	46.6 (7.9)
TIA (n = 12)	41.1 (6.8)	41.5 (9.6)	41.7 (8.1)	41.3 (6.0)	41.8 (3.9)
I/TIA (n = 16)	32.3 (4.5)**	29.4 (7.0)**	28.6 (5.2)**	29.6 (5.1)**	32.4 (4.5)**
PD (n = 10)	34.4 (4.9)	33.9 (5.4)	32.6 (5.7)	31.9 (4.6)	36.3 (4.4)
H (n = 12)	39.3 (6.2)	38.1 (5.6)	37.0 (5.9)	36.8 (7.0)	39.7 (8.6)
CBV (ml/100 g)					
Normal	3.29 (0.44)	2.94 (0.47)	3.14 (0.68)	3.31 (0.36)	3.70 (0.44)
NS	4.95 (0.83)	5.08 (1.03)**	5.13 (0.84)**	4.77 (0.84)	5.09 (0.66)
TIA	6.36 (1.40)**	6.36 (1.34)**	6.42 (1.59)**	6.24 (1.37)**	6.21 (1.25)*
I/TIA	5.90 (1.74)**	6.02 (1.87)**	6.30 (1.95)**	6.44 (1.64)**	6.49 (1.59)**
PD	4.81 (0.79)	4.70 (0.65)**	4.67 (0.98)	4.64 (1.11)	4.88 (0.98)
H	4.72 (1.16)	4.76 (0.80)**	4.79 (0.92)*	4.34 (0.66)	4.54 (0.71)
OEF (%)					
Normal	41.5 (4.4)	42.8 (4.5)	42.5 (4.6)	44.1 (3.8)	43.3 (4.9)
NS	42.3 (3.8)	42.4 (3.7)	42.6 (3.5)	43.5 (4.6)	42.1 (4.2)
TIA	47.1 (9.1)	49.1 (7.1)*	47.7 (7.7)	48.8 (6.1)	47.6 (6.9)
I/TIA	53.3 (9.2)**	53.7 (9.1)**	52.2 (8.9)**	51.9 (5.6)*	51.7 (5.0)**
PD	42.8 (4.2)	42.5 (4.5)	42.2 (4.4)	43.7 (4.7)	42.0 (4.7)
H	44.8 (7.6)	45.0 (6.6)	44.3 (6.4)	46.5 (6.6)	43.4 (7.6)
$CMRO_2$ (ml/min/100 g)					
Normal	3.36 (0.49)	3.39 (0.52)	3.29 (0.54)	3.43 (0.52)	3.59 (0.62)
NS	3.30 (0.27)	3.28 (0.34)	3.18 (0.45)	3.30 (0.42)	3.45 (0.35)
TIA	3.28 (0.60)	3.41 (0.56)	3.41 (0.83)	3.46 (0.62)	3.39 (0.43)
TIA/I	2.93 (0.29)	2.69 (0.43)*	2.56 (0.36)*	2.66 (0.46)**	2.89 (0.37)**
PD	2.57 (0.36)*	2.54 (0.31)**	2.42 (0.32)**	2.52 (0.52)**	2.72 (0.48)**
H	2.92 (0.22)	2.83 (0.19)*	2.69 (0.24)*	2.80 (0.28)	2.86 (0.39)*
MTT (s)					
Normal	4.77 (1.03)	4.34 (0.90)	4.69 (0.83)	5.05 (1.13)	5.25 (1.20)
NS	6.72 (1.83)	7.01 (2.20)	7.45 (2.11)	6.74 (1.76)	6.70 (1.30)
TIA	9.41 (2.02)**	9.39 (2.45)**	9.36 (2.23)**	9.16 (1.97)**	9.01 (2.19)
I/TIA	10.9 (2.66)**	12.6 (4.03)**	13.2 (3.24)**	13.4 (3.98)**	12.4 (4.20)**
PD	8.51 (1.43)*	8.50 (1.76)**	8.68 (1.44)*	8.86 (2.34)**	8.20 (2.39)
H	7.25 (1.61)	7.58 (1.46)	7.97 (2.04)	7.21 (1.21)	7.11 (1.66)

Values are mean (SD) for regional variables in all patients. General linear model regression analysis for each variable (CBF, CBV, OEF, $CMRO_2$, MTT) was undertaken to determine whether there was a significant increase or decrease in disease groups compared with the normal control group. As the age distribution was different between the groups, the "age" effect was included in the model. Bonferroni's correction for multiple comparisons was applied for 45 contrasts for each variable and the level of significance was set at $p<0.05$. Statistical analysis was carried out after some preprocessing to justify the normality of the residuals, as stated in Methods.

*$p<0.05$, **$p<0.01$ v normal controls.

CBF, cerebral blood flow; CBV, cerebral blood volume; $CMRO_2$, cerebral metabolic rate for oxygen; H, intracerebral haemorrhage group; MTT, mean transit time; normal, normal control; NS, non-symptomatic group; OEF, oxygen extraction fraction; PD, permanent deficit group; TIA, transient ischaemic attack without infarction group; TIA/I, transient ischaemic attack with infarction group.

Symptomatic patients

Symptomatic patients were categorised into *ischaemic* or *haemorrhagic* types. The haemorrhagic group (H group; mean age 33 years, range 15 to 53) consisted of 12 patients with the initial symptoms of haemorrhage. These patients had well preserved activities of daily living after intraventricular bleeding or a minor intracerebral haemorrhage. These patients were examined no sooner than four months after the onset of symptoms. Patients with a severe deficit after massive parenchymal damage were not included in the current series.

Patients with ischaemic onset were further categorised according to whether or not they complained of transient ischaemic attacks (TIA) when they were referred to our clinic. Symptoms in patients with TIA included motor, sensory, visual, or language deficits which resolved within 24 hours. Twelve patients with TIA were free from infarcted lesions on T2 weighted MRI done before the PET study and were categorised as *pure TIA* (TIA group; mean age 24 years, range 12 to 40). The other 16 patients had infarcted lesions on T2 weighted MRI and were categorised as the *TIA with infarction* (I/TIA group; mean age 37 years, range 13 to 64). The other ischaemic patients had permanent deficits such as motor or language deficit or disturbed higher cerebral function detected by intelligence or memory tests, but were free from TIA. In these patients the interval between the initial interview and the PET measurement was two months at most. All these patients had infarcted lesions on MRI and were categorised as having *permanent deficit because of cerebral infarction* (PD group, n = 10; mean age 37 years, range 19 to 53).

Patient data were compared with those of normal volunteers with normal MRI and no history of neurological disorder (control group, n = 6; mean age 49 years, range 20 to 66).

All study protocols were approved by the ethics committee of the Tokyo Metropolitan Institute of Gerontology. All participants gave their written consent after being informed of the details of the study, including the objective of the measurements, the duration of the study, the amount of radiation exposure, and the blood sampling involved. In the case of patients under 20 years of age or those with mental or memory deficit, written consent was given by parents or appointed attendants.

PET measurement

The PET study was carried out using a Headtome-IV scanner (Shimadzu Corporation, Kyoto, Japan). An arterial catheter

Table 2 Regional data for occipital cortex and basal ganglia

	Occipital	Caudate/putamen	Thalamus	Cerebellum
CBF (ml/min/100 g)				
Normal (n=6)	46.5 (10.7)	43.9 (10.9)	37.5 (6.5)	47.8 (7.0)
NS (n=7)	47.4 (5.5)	46.5 (8.7)	43.2 (7.7)	59.6 (8.9)
TIA (n=12)	43.3 (7.1)	45.0 (6.5)	42.6 (5.9)	49.7 (6.4)
TIA/I (n=16)	36.3 (6.4)**	36.2 (5.3)	35.8 (4.4)	55.9 (7.1)
PD (n=10)	38.3 (6.1)	37.8 (5.6)	36.6 (5.3)	49.7 (6.0)
H (n=12)	40.6 (7.3)	39.0 (9.0)	35.6 (4.8)	49.5 (7.1)
CBV (ml/100 g)				
Normal	3.89 (0.23)	3.13 (0.52)	3.58 (0.74)	4.09 (0.58)
NS	4.94 (0.48)	4.43 (1.01)	4.53 (1.15)	4.09 (0.15)
TIA	6.12 (1.17)	5.62 (1.72)**	4.87 (1.12)	4.12 (0.48)
TIA/I	6.25 (1.83)*	5.59 (1.66)**	4.83 (1.47)	4.12 (0.63)
PD	5.25 (0.92)	4.17 (0.65)	4.57 (0.85)	4.05 (0.64)
H	4.36 (0.83)	4.28 (0.99)	4.29 (1.58)	4.04 (0.64)
OEF (%)				
Normal	43.8 (5.6)	43.1 (4.5)	39.3 (5.8)	42.5 (6.3)
NS	42.7 (4.8)	43.0 (5.0)	38.8 (5.3)	38.1 (5.8)
TIA	47.3 (6.4)	46.3 (4.9)	41.0 (5.6)	41.5 (6.9)
TIA/I	48.0 (5.2)	49.1 (4.0)	41.2 (6.6)	42.3 (5.3)
PD	40.7 (4.5)	41.7 (3.5)	34.9 (5.5)	37.7 (4.5)
H	44.2 (6.1)	44.2 (5.6)	37.0 (7.2)	40.2 (6.9)
$CMRO_2$ (ml/min/100 g)				
Normal	3.84 (0.58)	3.56 (0.52)	2.82 (0.50)	3.87 (0.51)
NS	3.49 (0.18)	3.38 (0.34)	2.88 (0.43)	3.83 (0.29)
TIA	3.49 (0.57)	3.51 (0.56)	2.93 (0.56)	3.85 (0.55)
TIA/I	2.97 (0.40)**	3.06 (0.35)	2.53 (0.35)	3.58 (0.39)
PD	2.80 (0.59)**	2.80 (0.54)*	2.26 (0.49)	3.31 (0.57)
H	2.90 (0.31)**	2.81 (0.47)*	2.19 (0.27)	3.19 (0.28)
MTT (s)				
Normal	5.24 (1.18)	4.48 (1.32)	5.82 (1.42)	5.23 (1.12)
NS	6.32 (0.88)	5.80 (1.18)	6.39 (1.58)	4.20 (0.70)
TIA	8.68 (1.94)	7.61 (2.33)	6.95 (1.77)	4.48 (0.68)
TIA/I	10.6 (3.55)**	9.26 (2.31)**	8.15 (2.53)	5.07 (1.16)
PD	8.41 (2.08)	6.82 (2.01)	7.57 (1.53)	4.89 (0.62)
H	6.62 (1.64)	6.75 (1.23)	7.34 (2.86)	5.02 (1.33)

Values are mean (SD) for regional variables in all patients. General linear model regression analysis for each variable (CBF, CBV, OEF, $CMRO_2$, MTT) was undertaken to determine whether there was a significant increase or decrease in disease groups compared with the normal control group. As the age distribution was different between the groups, the "age" effect was included in the model. Bonferroni's correction for multiple comparisons was applied for 45 contrasts for each variable and the level of significance was set at $p<0.05$. Statistical analysis was carried out after some preprocessing to justify the normality of the residuals, as stated in Methods.

*$p<0.05$, **$p<0.01$ *v* normal controls.

CBF, cerebral blood flow; CBV, cerebral blood volume; $CMRO_2$, cerebral metabolic rate for oxygen; H, intracerebral haemorrhage group; MTT, mean transit time; normal, normal control; NS, non-symptomatic group; OEF, oxygen extraction fraction; PD, permanent deficit group; TIA, transient ischaemic attack without infarction group; TIA/I, transient ischaemic attack with infarction group.

was inserted into the radial artery for blood sampling. The transmission data were acquired with a rotating germanium-68 rod source for attenuation correction.

The regional cerebral blood flow (CBF), cerebral metabolic rate of oxygen ($CMRO_2$), and oxygen extraction fraction (OEF) were measured using continuous and consecutive nine minute inhalations of $C^{15}O_2$ and $^{15}O_2$ gas with continuous arterial blood sampling, employing a table-lookup technique.[12 13] The regional CBF and OEF were calculated with lookup tables created from the arterial whole blood and plasma radioactivity curves, and corrected for delay and dispersion.[14] The cerebral blood volume (CBV) was measured by a three minute inhalation of $C^{15}O$ with blood sampling.[15] The OEF was corrected for the effect of the regional CBV.[16] The mean transit time (MTT) was calculated as CBV/CBF.

PET data analysis

All the PET data were analysed using the image analysis software system "Dr View" (Asahi Kasei Joho System Company, Tokyo, Japan). The regions of interest (ROI) were manually placed over the cerebellar cortex, lower and upper frontal cortex, temporal cortex, occipital cortex, parietal cortex, sensorimotor cortex (mainly of the hand area) (targeted to premotor, primary motor, and primary sensory cortex), putamen, and thalamus. Each of the cortical ROIs consisted of a series of 1 cm diameter circles along the cortical rim. Putaminal and thalamic ROIs were a 2×3 cm ellipse and a 2 cm diameter circle, respectively. The ROIs were placed using a brain atlas,[17] avoiding the infarcted areas.

In the analysis of patient data, the ROI values were analysed in the cerebral hemisphere with the lower CBF, as the pathology in the hemisphere under more severe haemodynamic stress determined the clinical manifestations in each patient. For normal controls, the mean of two hemispheric values was taken for each subject. The data obtained are expressed as mean (SD) for each patient group and the controls.

Statistical analysis

Differences between the groups were examined. A general linear model regression analysis, which is an expansion of analysis of covariance (ANCOVA), was undertaken for each of the five variables (CBF, CBV, OEF, $CMRO_2$, MTT) as the dependent variable, using a model that consisted of the intercept, the effect of "group" (five kinds of disease state plus control), the effect of "region" (nine regions), the interaction between group and region, and age as covariates. Age was included in the model because the age distribution

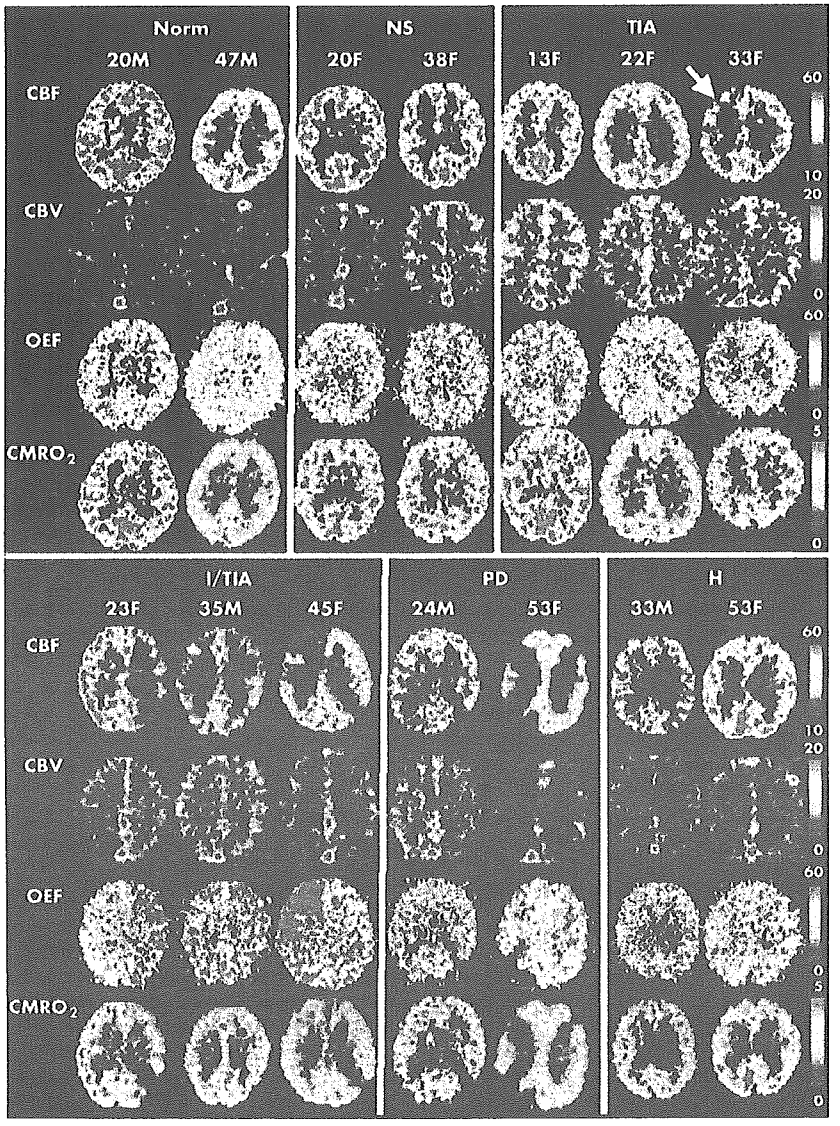

Figure 1 Positron emission tomographic images of two or three representative patients from each of the five patient groups and the normal control group are shown using the same colour scale. A slice including the bodies of the lateral ventricles is displayed for each subject. The intergroup differences in cerebral blood flow (CBF), cerebral blood volume (CBV), oxygen extraction fraction (OEF), and cerebral metabolic rate for oxygen ($CMRO_2$) expressed in table 1 are well shown in these images. CBV was higher in the NS group than in the controls, and higher in the TIA group than in the NS group, although CBF showed no apparent difference among the three groups. Some patients in the TIA group had focally decreased CBF, as exemplified in the third patient (arrowed). The OEF values in these regions were somewhat higher than in the rest of the brain. However, the increase in OEF was more prominent in patients in the I/TIA group. Patients in the PD group had extensive infarction, and the OEF in non-infarcted areas was not increased. Patients in the H group did not have increased OEF, and the CBV increase was as mild as in the NS and PD groups. H, patients with haemorrhagic onset; I/TIA, patients with TIA plus infarction; Norm, normal control; NS, non-symptomatic patients; PD, patients with infarction and permanent neurological deficit; TIA, patients with TIA without infarction.

was different between the groups. Contrasts were made on the group by region interaction effects to test the difference between the normal controls and each of the five disease states for each region, making a total of 45 contrasts for each variable. Bonferroni's correction was applied for multiple comparisons, and the level of significance was set at $p<0.05$. This statistical analysis is similar to an ANCOVA for each region independently, but is more powerful because the error is estimated from the data for all regions. To justify *t* tests and F tests, normality was checked for the residuals in each test. A few outliers (for each subject for CBF, CBV, and OEF analysis) were removed, and the remaining data were tested again. As for the CBV values, log transformation was applied before the statistical analysis because CBV had a skewed distribution owing to augmentation of the vasculature by moyamoya vessels. As a result, normality of the residuals was confirmed for every test carried out in this study. Exclusion of the outliers did not change the statistical results.

Next, the correlation among the variables was examined by plotting the mean values among CBF, CBV, and OEF for each group. This analysis was undertaken on the lower and upper frontal cortex, the region considered to be most commonly affected in Moyamoya disease. To test for significant differences between the groups in the multivariate space

and to examine the correlations among the variables, a multivariate analysis of covariance was carried out for the vectors of three dimensions (CBF, CBV, and OEF) as the dependent variable, using a model that consisted of the intercept, the effect of group, the effect of region, and age as covariates This model was used after confirming that the interaction between region and group was not significant among these frontal regions. $CMRO_2$ was not included among the dependent variables because of possible dependence among CBF, OEF, and $CMRO_2$. MTT was not included in the analysis as it is calculated from CBV/CBF. Contrasts were made on the "group" effects to test for the difference between every possible pair among the six groups—making a total of 15 contrasts—by F tests with Wilks's λ. For this multivariate analysis, normality was checked for the residuals for three variables after prepreprocessing, as stated in general linear regression analysis (exclusion of three outliers and log transformation of CBV data). Bonferroni's correction was applied for multiple comparisons, and the level of significance was set at $p<0.05$. The residual correlation coefficient was evaluated to examine the correlation among the variables after correcting for age, group, and region.

The statistical analyses were done using the JMP statistical software package (SAS Institute Inc, Cary, North Carolina, USA).

RESULTS

ROI analysis and PET images

Table 1 gives the results of general linear model regression analysis for each variable (CBF, CBV, OEF, $CMRO_2$, and MTT), showing a significant increase or decrease in the disease groups compared with the normal control group (tables 1 and 2).

CBF in NS, TIA, PD, and H groups was not significantly lower than in the normal controls in any region, but in the I/TIA group the difference reached significance in many cerebral regions.

CBV in NS, PD, and H groups was higher than in the normal controls in all cerebral ROIs, and significantly so in the frontal cortex. The increase in CBV in the TIA and I/TIA groups was much more marked than in the other patient groups and was statistically significant in most cerebral regions. The increase was more than double the control value in the upper frontal and sensorimotor regions.

$CMRO_2$ in the PD group was lower than in the controls in all regions except the thalamus and cerebellum. $CMRO_2$ in the I/TIA and H groups was also decreased significantly in some areas within many of the cerebral regions. The degree of decrease was greatest in the PD group throughout all areas of the cerebral cortex.

An increase in the OEF was found in the frontal, parietal, and temporal cortex in the I/TIA group compared with the normal controls. The OEF in the TIA group was the second largest in all regions; it was significantly different from the controls in the upper frontal region.

In all regions except the thalamus and cerebellum, mean MTT ranged from shortest to longest in the following order: normal control, NS, H, PD, TIA, and I/TIA. MTT was significantly longer in the I/TIA group than in the controls in all these regions. MTT in NS group was longer than in the controls, but the difference was not significant in any region.

None of the measured variables showed any difference from control values in the thalamus and cerebellum (areas rarely affected in moyamoya disease) in any of the subgroups.

Figure 1 shows PET images of representative patients from each of the five patient groups and the normal control group. The haemodynamic characteristics of each group are expressed in a side by side comparison of the images (see legend for detail).

Analysis of correlations among multiple factors

In order to interpret the pathophysiological features of cerebrovascular disease, it is necessary not only to clarify the alteration of single factors but also the altered coupling of multiple factors. In this study, the variation in haemodynamics was most prominently observed in the frontal cortex (table 1). Thus we plotted the means of the two frontal regions (lower and upper) in the three graphs shown in fig 2, panels A to C. Graph 1 (panel A) plots the correlation between CBF and CBV; graph 2 (panel B) plots that between CBF and OEF; and graph 3 (panel C) plots that between OEF and CBV. In all these graphs, the regions belonging to the same subtypes had closely similar plots.

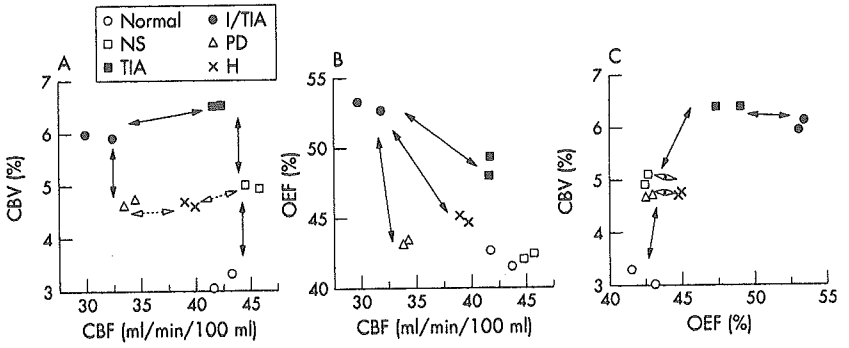

Figure 2 Two dimensional plots of the correlations between the cerebral blood flow (CBF; x axis) and cerebral blood volume (CBV; y axis) (panel A), CBF (x axis) and oxygen extraction fraction (OEF; y axis) (panel B), and OEF (x axis) and CBV (y axis) (panel C). The means of two frontal regions among all the subjects are plotted. To test for significant differences between the groups (CBF, CBV, OEF) in three dimensional multivariate space, a multivariate analysis of covariance was carried out. This analysis showed a significant difference between every possible pair among the six groups except NS *v* H, and PD *v* H. In these graphs, significant and non-significant intergroup differences, as given in Results, are indicated by arrows with black and white heads, respectively. Among all subtypes, the I/TIA group had maximally increased CBV and OEF in the range of decreased CBF. The TIA group had maximal CBV and an increase in the OEF that was somewhat less than in the I/TIA group. The means of the NS, PD, and H groups were closely similar in all the graphs, and the degree of haemodynamic stress was milder in these groups than in the I/TIA and TIA groups. H, patients with haemorrhagic onset; I/TIA, patients with TIA plus infarction; Normal, normal control; NS, non-symptomatic patients; PD, patients with infarction and permanent neurological deficit; TIA, patients with TIA without infarction.

To test for significant differences between the groups in multivariate space, a multivariate analysis of covariance was carried out for the vectors of the three dimensions (CBF, CBV, OEF) as the dependent variable, as stated in Methods. This analysis showed a significant difference between every possible pair among the six groups except NS *v* H and PD *v* H, suggesting important variations in the pathophysiological state in moyamoya disease. The correlation coefficients among the residuals were low (−0.021 for CBF *v* log CBV, −0.354 for CBF *v* OEF, and 0.064 for log CBV *v* OEF), supporting the effectiveness of the multivariate analysis on the three variables.

Figure 2A plots the correlation between CBF and CBV. CBV was higher in the NS group than in the normal controls, but the ranges of CBF did not differ between these groups. CBV was even higher in the TIA group and the difference was significant, but the CBF range was still within that of the control and NS groups. CBF in the I/TIA group was lower than in the TIA group within a similar CBV range, and CBV in the PD group was lower than that in the I/TIA group within the same CBF range. The H group lay between NS and PD, and there was no significant difference in multivariate distribution between H and NS, and H and PD.

Figure 2B plots the correlation between CBF and OEF. In this plot, the I/TIA group had a significantly raised OEF in the range of decreased CBF, and this group had a different multivariate distribution compared with all the other patient groups and normal controls.

Figure 2C plots the correlation between OEF and CBV. Groups NS, PD, and H were distributed similarly, and there was no significant difference in multivariate distribution between NS and H, or H and PD. CBV in these three groups was higher than the normal controls within the similar OEF range. CBV in the TIA group was raised even further. The range of OEF in the TIA group extended slightly rightward along the highly increased CBV range. The OEF of the I/TIA group was even higher than in the TIA group within a similar CBV range.

DISCUSSION

Characteristics of haemodynamic factors and clinical presentation

In this paper we have shown that there are differences in haemodynamic characteristics among the various clinical presentations of moyamoya disease. This may have important implications for the evolution of the disease, as well as helping to determine the appropriate treatment for a particular patient.

Even asymptomatic patients (the NS group) had a raised CBV compared with normal controls, and the difference was significant in the upper frontal and sensorimotor cortices. Though this indicated a perfusion pressure below normal, the prolonged asymptomatic period without any infarction suggests that perfusion had not fallen far enough to elicit an ischaemic event. CBV in the patients with TIA without infarction (the TIA group) was double that of the normal controls within the same resting CBF range, and the patients developed TIAs under these conditions. This CBV value may indicate the limit of vasodilator compensation needed to preserve resting flow. It was interesting that the ischaemic event occurred when the resting CBF was in the normal range. This paradoxical finding suggests that CBF may decline below the resting condition and reach the ischaemic range when some physiological stress is added. Such a paradoxical steal phenomenon is observed in the blood flow tolerance test when the vascular bed is maximally dilated and autoregulation completely lost.[18 19]

In patients with TIA symptoms plus lesions (the I/TIA group), a marked increases in the OEF together with a TIA event is strongly suggestive of further deterioration. The MTT—a variable that should have an inverse relation with cerebral perfusion pressure—was larger in the I/TIA patients than in any of the other groups; hence the haemodynamic compromise in this group was the severest among all the patient groups.

Once the permanent deficit had occurred and stabilised (the PD group), CBV in the non-infarcted area decreased from the range found in the I/TIA patients, as shown in fig 2A. The decreased demand for oxygen delivery is thought to lead to a decrease in the vascular bed, thereby resulting in a return of the OEF value to the normal range, as indicated in fig 2B.

The haemodynamic status of the haemorrhagic cases (the H group) should be considered in a different context, as the cause of deterioration is not an ischaemic event. Most patients with haemorrhagic onset are symptom-free until just before the event. The regional mean values in the H group were closely similar to those of the NS group in the graphs in fig 2. However, many cortical and basal regions in the H group showed significantly decreased $CMRO_2$. Thus it is reasonable to assume that functional deterioration caused by the haemorrhage is the main feature of the H group, and that the degree of haemodynamic stress of H patients is generally as moderate as in NS patients. Multivariate correlation analysis also supports this hypothesis, as the three dimensional (CBF, CBV, OEF) vector of the H group was not significantly different from the NS and PD groups.

Significance of graded haemodynamics for patient management

Clinical management of patients with moyamoya disease should be individualised on the basis of the haemodynamic stress evidenced by assessment of CBF, CBV, OEF, and MTT. At the same time it is clear that there are some common correlations between the clinical presentation and the level of haemodynamic stress. Thus far, there have been no reliable follow up studies of moyamoya disease based primarily on haemodynamic data. However, the risk of further deterioration from ischaemic events can be inferred using the more widely investigated natural course of chronic atherosclerotic carotid occlusion[20 21] as a reference.

The I/TIA type is characterised by an increased OEF in the dimension of markedly increased CBV. This may constitute justification for carrying out surgical revascularisation in I/TIA patients, given that there is a high risk of further stroke.[20 21] The NS, PD, and H patients with normal OEF values and only moderately increased CBV and MTT may not be at high stroke risk in the near future.[21 22] The haemodynamic conditions occurring in the TIA group cannot be considered an analogue of atherosclerotic carotid disease, as a highly increased CBV in the normal or only mildly increased OEF range is rarely observed in atherosclerotic patients.[21] In practice, these patients often undergo operations because they present with transient ischaemic symptoms of a type that can be effectively ameliorated by surgical revascularisation. Thus to determine the optimal treatment for this type of patients, we may need to consider not only the stroke risk in the immediate future, but also the possibility of functional amelioration by treatment, the long term benefits for younger patients, and the possible worsening of the haemodynamic state because of progressive occlusion of the carotid artery. As the natural history of treated and untreated patients with moyamoya disease is less clear than in atherosclerotic disease, long term follow up of these patients is necessary. Assessment of the subjects' haemodynamic condition will be mandatory in such studies in order to compare the natural course of the disease and the effectiveness of treatment among the patient groups.

We also propose that the management of each patient should be determined by their haemodynamic condition. Although PET information is of greatest value in assessing this, it is not usually available in daily clinical practice. Thus, establishment of more easily accessible alternative methods for measuring the degree of haemodynamic stress is necessary. Acetazolamide challenge using quantitative CBF measurement[23] and perfusion weighted MRI[24] may be the best candidates for this purpose. Evaluation of the same patient groups using PET, acetazolamide challenge, and perfusion MRI may be necessary to clarify the value of each method.

Authors' affiliations

T Nariai, Y Matsushima, S Imae, Y Tanaka, K Ohno, Department of Neurosurgery, Tokyo Medical and Dental University, Tokyo, Japan
K Ishii, Positron Medical Centre, Tokyo Metropolitan Institute of Gerontology
M Senda, Department of Image Based Medicine, Institute of Biomedical Research and Innovation, Kobe, Japan

Competing interests: none declared

REFERENCES

1 **Suzuki J**, Takaku A. Cerebrovascular "moyamoya" disease. Disease showing abnormal net-like vessels in base of brain. *Arch Neurol* 1969;**20**:288–99.
2 **Matsushima Y.** Moyamoya disease. In: Youmans J, eds. *Neurological surgery: a comprehensive reference guide to the diagnosis and management of neurosurgical problems*, 4th ed. Philadelphia: WB Saunders, 1996:1202–23.
3 **Matsushima Y.** Moyamoya disease. In: Albright A, Pollack I, Adelson P, eds. *Principles and practice of pediatric neurosurgery*. New York: Thieme, 1999:1053–69.
4 **Matsushima Y**, Aoyagi M, Niimi Y, *et al.* Symptoms and their pattern of progression in childhood moyamoya disease. *Brain Dev* 1990;**12**:784–9.
5 **Ikezaki K**, Matsushima T, Kuwabara Y, *et al.* Cerebral circulation and oxygen metabolism in childhood moyamoya disease: a perioperative positron emission tomography study. *J Neurosurg* 1994;**81**:843–50.
6 **Tagawa T**, Naritomi H, Mimaki T, *et al.* Regional cerebral blood flow, clinical manifestations, and age in children with moyamoya disease. *Stroke* 1987;**18**:906–10.
7 **Touho H**, Karasawa J, Ohnishi H. Preoperative and postoperative evaluation of cerebral perfusion and vasodilatory capacity with 99mTc-HMPAO SPECT and acetazolamide in childhood Moyamoya disease. *Stroke* 1996;**27**:282–9.
8 **Suzuki R**, Matsushima Y, Takada Y, *et al.* Changes in cerebral hemodynamics following encephalo-duro-arterio-synangiosis (EDAS) in young patients with moyamoya disease. *Surg Neurol* 1989;**31**:343–9.
9 **Nariai T**, Suzuki R, Matsushima Y, *et al.* Surgically induced angiogenesis to compensate for hemodynamic cerebral ischemia. *Stroke* 1994;**25**:1014–21.
10 **Roach ES.** Immediate surgery for moyamoya syndrome? Not necessarily. *Arch Neurol* 2001;**58**:130–1.
11 **Scott RM.** Surgery for moyamoya syndrome? Yes. *Arch Neurol* 2001;**58**:128–9.
12 **Senda M**, Buxton RB, Alpert NM, *et al.* The ^{15}O steady-state method; correction for variation in arterial concentration. *J Cereb Blood Flow Metab* 1988;**8**:681–90.
13 **Sadato N**, Yonekura Y, Senda M, *et al.* PET and the autoradiographic method with continuous inhalation of oxygen-15-gas: theoretical analysis and comparison with conventional steady-state methods. *J Nucl Med* 1993;**34**:1672–80.
14 **Iida H**, Kanno I, Miura S, *et al.* Error analysis of a quantitative cerebral blood flow measurement using $H_2(15)O$ autoradiography and positron emission tomography, with respect to the dispersion of the input function. *J Cereb Blood Flow Metab* 1986;**6**:536–45.
15 **Grubb R**, Raichle M, Higgins C, *et al.* Measurement of regional cerebral blood flow by positron emission tomography. *Ann Neurol* 1978;**4**:322–8.
16 **Lammertsma AA**, Jones T, Frackowiack RS, *et al.* Correction for the presence of intravascular oxygen extraction ratio in the brain. *J Cereb Blood Flow Metab* 1983;**3**:416–24.
17 **Talairach J**, Tournoux P. Horizontal sections. In: *Co-planar stereotaxic atlas of human brain. 3-dimensional proportional system: an approach to cerebral imaging*. New York: Thieme, 1988:81–110.
18 **Nariai T**, Senda M, Ishii K, *et al.* Posthyperventilatory steal response in chronic cerebral hemodynamic stress: a positron emission tomography study. *Stroke* 1998;**29**:1281–92.
19 **Yonas H**, Smith HA, Durham SR, *et al.* Increased stroke risk predicted by compromised cerebral blood flow reactivity. *J Neurosurg* 1993;**79**:483–9.
20 **Grubb RL**, Derdeyn CP, Fritsch SM, *et al.* Importance of hemodynamic factors in the prognosis of symptomatic carotid occlusion. *JAMA* 1998;**280**:1055–60.
21 **Derdeyn CP**, Videen TO, Yundt KD, *et al.* Variability of cerebral blood volume and oxygen extraction: stages of cerebral haemodynamic impairment revisited. *Brain* 2002;**125**:595–607.
22 **Powers WJ**, Tempel LW, Grubb RL. Influence of cerebral hemodynamics on stroke risk: one-year follow-up of 30 medically treated patients. *Ann Neurol* 1989;**25**:325–30.
23 **Nariai T**, Suzuki R, Hirakawa K, *et al.* Vascular reserve in chronic cerebral ischemia measured with acetazolamide challenge test: comparison with positron emission tomography. *Am J Neuroradiol* 1995;**16**:563–570.
24 **Calamante F**, Ganesan V, Kirkham FJ, *et al.* MR perfusion imaging in moyamoya syndrome: potential implications for clinical evaluation of occlusive cerebrovascular disease. *Stroke* 2001;**32**:2810–16.

Available online at www.sciencedirect.com

SCIENCE DIRECT

Nuclear Medicine and Biology 32 (2005) 253–262

NUCLEAR MEDICINE — AND — BIOLOGY

www.elsevier.com/locate/nucmedbio

Preclinical and clinical evaluation of *O*-[^{11}C]methyl-L-tyrosine for tumor imaging by positron emission tomography

Kiichi Ishiwata[a,*], Hideo Tsukada[b], Kazuo Kubota[c], Tadashi Nariai[d], Norihiro Harada[c], Kazunori Kawamura[a,e], Yuichi Kimura[a], Keiichi Oda[a], Ren Iwata[f], Kenji Ishii[a]

[a]*Positron Medical Center, Tokyo Metropolitan Institute of Gerontology, Itabashi-ku, Tokyo 173-0022, Japan*
[b]*Central Research Laboratory, Hamamatsu Photonics K.K., Hamakita 434-8601, Japan*
[c]*Department of Radiology, Division of Nuclear Medicine, International Medical Center of Japan, Shinjuku-ku, Tokyo 162-8655, Japan*
[d]*Department of Neurosurgery, Tokyo Medical and Dental University, Bunkyo-ku, Tokyo 113-8519, Japan*
[e]*SHI Accelerator Service Ltd., Shinagawa-ku, Tokyo 141-8686, Japan*
[f]*CYRIC, Tohoku University, Aoba-ku, Sendai 980-8578, Japan*

Received 25 August 2004; received in revised form 26 October 2004; accepted 10 November 2004

Dedicated to Professor Dr. Willem Vaalburg on the occasion of his retirement (K.I.).

Abstract

We performed preclinical and clinical studies of *O*-[^{11}C]methyl-L-tyrosine, a potential tracer for imaging amino acid transport of tumors by positron emission tomography (PET). Examinations of the radiation-absorbed dose by *O*-[^{11}C]methyl-L-tyrosine and the acute toxicity and mutagenicity of *O*-methyl-L-tyrosine showed suitability of the tracer for clinical use. The whole-body imaging of monkeys and healthy humans by PET showed low uptake of *O*-[^{11}C]methyl-L-tyrosine in all normal organs except for the urinary track and bladder, suggesting that the *O*-[^{11}C]methyl-L-tyrosine PET has the potential for tumor imaging in the whole-body. Finally, the brain tumor imaging was preliminarily demonstrated.

Keywords: *O*-[^{11}C]methyl-L-tyrosine; Tumor imaging; Positron emission tomography

1. Introduction

For tumor diagnosis by positron emission tomography (PET), 2-deoxy-2-[^{18}F]fluoro-D-glucose ([^{18}F]FDG) is of first choice of radiopharmaceuticals worldwide. The whole-body imaging with the [^{18}F]FDG PET is routinely performed for tumor imaging; however, its limitations are well understood [1]. For example, high uptake of [^{18}F]FDG in the normal brain tissues hampers the tumor imaging in the brain. Uptake in the inflammatory tissues is sometimes troublesome for differential diagnosis [2]. Excretion of [^{18}F]FDG through the urinary track also sometimes makes tumor diagnosis difficult in a lower abdominal region. In contrast to [^{18}F]FDG, radiolabeled amino acids are taken in the normal brain tissue at much lower levels, which enables imaging of the majority of low- and high-grade brain tumors. Uptake of L-[*methyl*-^{11}C]methionine in the inflammatory tissues was low [3]. A variety of radiolabeled amino acids were prepared and evaluated, as reviewed by Vaalburg et al. [4] and Jager et al. [5]. So far, L-[*methyl*-^{11}C]methionine is widely used in most clinical studies because of its simple and efficient labeling procedure. The metabolism of L-[*methyl*-^{11}C]methionine was complicated for the kinetic modeling, whereas L-[1-^{11}C]tyrosine can be used for measuring the protein synthesis rate. On the other hand, the metabolically stable artificial amino acids are also available for evaluating the amino acid transport in the tumors.

In contrast to brain tumor imaging, the use of radiolabeled amino acids for the tumor diagnosis in the abdominal region was limited, because many amino acids including both natural and artificial ones are physiologically taken at high levels in abdominal organs such as the pancreas, liver, small intestine and kidney in experimental animals. By the whole-body imaging technique, high uptake of L-[*methyl*-^{11}C]methionine or L-[1-^{11}C]tyrosine in the liver and pancreas was

* Corresponding author. Tel.: +81 3 3964 3241; fax: +81 3 3964 2188.
E-mail address: ishiwata@pet.tmig.or.jp (K. Ishiwata).

0969-8051/$ – see front matter © 2005 Elsevier Inc. All rights reserved.
doi:10.1016/j.nucmedbio.2004.11.005

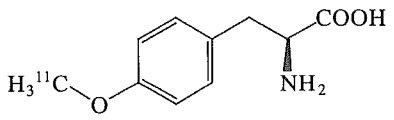

Fig. 1. Chemical structure of *O*-[^{11}C]methyl-L-tyrosine.

confirmed in humans [1,5]. However, Wester et al. [6] demonstrated very low uptake of the radioactivity in the pancreas and liver of humans after injection of *O*-[^{18}F]fluoroethyl-L-tyrosine, in spite of very high uptake of the tracer in the mouse pancreas. This artificial amino acid was originally developed as a tracer for imaging amino acid transport based on the concept that the longer half-life of ^{18}F (109.8 min compared to 20.4 min for ^{11}C) allows a single production to be sufficient for several patients, or alternatively, to be delivered to satellite PET centers. Other [^{18}F]fluorinated amino acids were also developed for the similar purpose: 4-[^{18}F]fluoro-L-phenylalanine [7], 4-[^{18}F]fluoro-L-proline [8], 1-amino-3-[^{18}F]fluorocyclobutane-1-carboxylic acid [9] and *O*-[^{18}F]fluoropropyl-L-tyrosine [10]. Recently, we also proposed *O*-[^{18}F]fluoromethyl-L-tyrosine, of which radiosynthesis is suitable for a large-scale routine production [11]. This amino acid and its ^{11}C-labeled counterpart, *O*-[^{11}C]methyl-L-tyrosine (Fig. 1), proved to be promising tracers for imaging amino acid transport in tumor tissues [12]. The short half-life of ^{11}C-labeled tracers has a potential disadvantage that the tracer is restrictedly used in a few subjects in PET centers with an on-site cyclotron; however, it in turn becomes a potential advantage that multiple tracers can be successively applied to the individual patients in the same day, that is, *O*-[^{11}C]methyl-L-tyrosine PET followed by [^{18}F]FDG PET, in addition to the low radiation-absorbed dose of the ^{11}C-labeled tracers compared with a longer half-lived ^{18}F tracers.

The aim of the present study is to confirm suitability of *O*-[^{11}C]methyl-L-tyrosine in clinical use. For this end, we evaluated the radiation dosimetry of *O*-[^{11}C]methyl-L-tyrosine for humans from the distribution data in mice and the acute toxicity and mutagenicity of *O*-methyl-L-tyrosine. Uptake of *O*-[^{11}C]methyl-L-tyrosine in the inflammatory tissue was compared to that in tumor tissue in a rat model [12,13]. To investigate the applicability of *O*-[^{11}C]methyl-L-tyrosine PET for tumor diagnosis in the whole-body, dynamic whole-body imaging with the *O*-[^{11}C]methyl-L-tyrosine, PET was preclinically performed in monkeys in addition to brain imaging. Clinically pharmacokinetics of *O*-[^{11}C]methyl-L-tyrosine was evaluated in three healthy subjects. Finally, the *O*-[^{11}C]methyl-L-tyrosine PET was applied to a patient with brain tumor.

2. Materials and methods

2.1. General

L-Tyrosine disodium salt was purchased from Research Biochemicals International (Natick, MA). *O*-Methyl-L-tyrosine was purchased from Bachem (Bubendorf, Switzerland). Male ddY mice and male Donryu rats were obtained from Tokyo Laboratory Animals (Tokyo, Japan). Two male rhesus monkeys (*Macaca mulatta*) were purchased from Japan SLC (Shizuoka, Japan).

The animal studies with rodents were approved by the Animal Care and Use Committee of the Tokyo Metropolitan Institute of Gerontology. The PET study with monkeys was performed at the Central Research Laboratory of Hamamatsu Photonics K.K., Hamamatsu, Japan, in accordance with recommendations of the US National Institute of Health and the guidelines of the Central Research Laboratory, Hamamatsu Photonics K.K. The clinical study was performed at the Positron Medical Center of the Tokyo Metropolitan Institute of Gerontology after approval by the institutional Ethical Committee.

2.2. Preparation of *O*-[^{11}C]methyl-L-tyrosine

O-[^{11}C]methyl-L-tyrosine was prepared by the reaction of L-tyrosine disodium and [^{11}C]methyl triflate by a slight modification of the reported procedure [11,12]. [^{11}C]Methyl triflate was bubbled into a solution of L-tyrosine disodium salt (2 mg/ml) in dimethylsulfoxide (0.5 ml) at room temperature. Then, the reaction mixture was diluted with 1.0 ml of water and applied to high-performance liquid chromatography (HPLC): column, YMC-Pack ODS-A column (10-mm inner diameter×250-mm length; particle size, 5 μm; YMC, Kyoto, Japan); mobile phase, CH_3CN/50 mM CH_3CO_2H/50 mM $CH_3CO_2NH_4$ (8:46:46, v/v/v); and flow rate, 5 ml/min. The fraction of *O*-[^{11}C]methyl-L-tyrosine (retention time, 7.0 min) was evaporated to dryness. The residue was dissolved in physiological saline and sterilized by membrane filtration. The radiochemical purity of *O*-[^{11}C]methyl-L-tyrosine was >97%, which was determined by HPLC: column, TSKgel super-ODS (4.6-mm inner diameter×100-mm length; particle size, 2 μm; Toso, Tokyo, Japan); mobile phase, CH_3CN/50 mM CH_3CO_2H/50 mM $CH_3CO_2NH_4$ (5:47.5:47.5, v/v/v); flow rate, 1 ml/min; and retention time, 3.6 min. The specific activity of *O*-[^{11}C]methyl-L-tyrosine was 41–118 TBq/mmol. Finally, the sterility and apyrogenicity of the products were confirmed.

2.3. Radiation dosimetry

O-[^{11}C]methyl-L-tyrosine (10 MBq/220 pmol) was intravenously injected into mice (8 weeks old, 34.4±0.5 g). They were killed by cervical dislocation 1, 5, 15, 30, 60 and 90 min after injection (n=4). The blood was collected by heart puncture, and the tissues were harvested. The samples were measured for the ^{11}C radioactivity with an autogamma counter and weighed. The tissue uptake of ^{11}C was expressed as a percentage of the injected dose per organ (%ID/organ) or a percentage of the injected dose per gram of tissue (%ID/g). Radiation dosimetry for human adults was estimated by the MIRD method based on the tissue distribution data of *O*-[^{11}C]methyl-L-tyrosine in mice as described previously [14].

2.4. Acute toxicity

Toxicity studies were performed at the Mitsubishi Chemical Safety Institute (Tokyo, Japan). Acute toxicity was assayed in Crj:CD(SD)IGS rats (SPF). *O*-Methyl-L-tyrosine at a dose of 2.41 mg per 12.3 μmol/kg body weight (1.0 mg/ml in physiological saline) was injected intravenously into 5-week-old rats weighing 164–174 and 132–145 g for males ($n=5$) and females ($n=5$), respectively. The dose of 2.41 mg/kg body weight is the 55 000-fold equivalent of the postulated administration dose (0.044 μg per 0.23 nmol/kg body weight) of 500 MBq *O*-[^{11}C]methyl-L-tyrosine with a specific activity of 37 TBq/mmol for humans weighing 60 kg. The three lots of *O*-[^{11}C]methyl-L-tyrosine prepared above were also assayed after decay-out of ^{11}C. Each of the three *O*-[^{11}C]methyl-L-tyrosine preparations was injected intravenously into 5-week-old male and female rats ($n=3$ for each) at doses of 4.1–5.8 μg per 21–30 nmol per 1.8–2.2 ml/kg body weight, which were 150-fold equivalent to the postulated administration dose of *O*-[^{11}C]methyl-L-tyrosine for humans. They were observed four times (0.5, 1, 3 and 6 h after the injection) at day 1 and thereafter once daily for clinical signs until 15 days, and weighed on days 4, 8 and 15. At the end of the 15-day observation period, the rats were euthanized and a macroscopic analysis was performed.

2.5. Ames test

Mutagenicity tests were performed at the Mitsubishi Chemical Safety Institute. *O*-Methyl-L-tyrosine was tested for mutagenicity in the Ames test with four histidine-requiring strains of *Salmonella typhimurium* (TA98, TA100, T1535 and T1537) at a dose range of 0.0763–5000 μg/plate by the standard method.

2.6. Uptake study in a rat inflammation model

AH109A ascitic hepatoma cells and turpentine oil were subcutaneously inoculated on the back of Donryu rats (6 weeks old) 8 and 4 days, respectively, before the uptake study [12,13]. *O*-[^{11}C]methyl-L-tyrosine (20 MBq/700 pmol) was intravenously injected into rats (210±13 g, $n=7$). They were killed by cervical dislocation 30 min after injection. The blood was collected by heart puncture, and AH109A, inflammatory tissue and muscle were harvested. The uptake of ^{11}C was expressed as a %ID/g as described above.

2.7. Monkey study

Positron emission tomography measurement was performed in two male monkeys (2.1 years old, 6.1 kg; and 1.7 years old, 5.1 kg). They were trained to sit on a chair twice a week for more than 3 months for PET measurement in the conscious state. The PET camera used was SHR-7700 (Hamamatsu Photonics K.K.), which has an axial field-of-view of 11.4 cm and acquires 31 slices at a center-to-center interval of 3.6 mm [15].

A conscious monkey (6.1 kg) was fixed on a PET camera, and transmission scanning with a rotating [^{68}Ge]/[^{68}Ga] line source was performed to correct for attenuation, then *O*-[^{11}C]methyl-L-tyrosine (1000 MBq/8.7 nmol) was injected through the posterior tibial vein cannula, and the PET scan was performed in the head in two-dimensional (2D) mode for 91 min (10 s×6 frames, 30 s×6 frames, 1 min×12 frames and 3 min×25 frames). Arterial blood samples were obtained 1, 5, 15, 30, 60 and 90 min after injection of the radiotracer. Whole blood and plasma were measured for the ^{11}C radioactivity and weighed, and the radioactivity levels were expressed as a standardized uptake value [SUV, (activity of sample/g of sample)/(total injected activity/g body weight)]. Metabolites in the plasma were analyzed by thin-layer chromatography (TLC) on Kieselgel 60 plates (Merck, Darmstadt, Germany) with *n*-butanol/acetic acid/water (4:1:2, v/v/v) as eluent as previously described [16]. A migration rate (R_f) of *O*-[^{11}C]methyl-L-tyrosine was 0.40.

In the other monkey (5.1 kg), the dynamic whole-body PET scan was performed in 2D mode in four overlapping bed positions covering from the neck to thighs. In this case, the monkey was anesthetized during PET scan. Anesthesia was induced with 10 mg/kg im injection of ketamine hydrochloride. The monkey was tracheostomized, immobilized with 0.05 mg/kg im injection of pancuronium bromide every 2 h and artificially ventilated. Anesthesia was continued with 0.8% isoflurane in a $N_2O/O_2/N_2$ (1:1:1, v/v/v) gas mixture during the entire experiment. Catheterization of the left femoral artery was then performed to measure mean arterial blood pressure and heart rate and for arterial blood sampling. During PET scans, heart rate, respiration rate and body temperature were continuously monitored using a life monitoring system (Nihon Kohden, Tokyo, Japan). The levels of carbon dioxide ($PaCO_2$), blood oxygen (PaO_2), pH and blood pressure of arterial blood were measured. Arterial blood samples were obtained at 30 and 90 min after the start of saline or ketamine infusion via a cannula in the femoral artery, and monitored with a Stat Profile blood gas analyzer (Nova Biochemical, Massachusetts).

Transmission scans were performed at every four bed positions with a 20-min scan per position for attenuation correction, and then each emission scan at the four positions was performed in Z-motion mode to provide 112 slices. After injection of *O*-[^{11}C]methyl-L-tyrosine (720 MBq/8.7 nmol), a set of 1-min scan at each of the four bed positions from the neck to thighs was repeated every 4 min over 92 min.

The tomographic images were reconstructed with a filtered backprojection method. The data were collected in a 256×256×122 matrix, and the voxel size was 1.2×1.2×3.6 mm. Voxel counts were calibrated to activity concentration (Bq/ml). Regions of interest (ROIs) were placed on the temporal cortex based on the MRI images in the first monkey and on the lung, heart, liver, pancreas, spleen, kidney and muscle in the second monkey. The decay-corrected time–activity curves of these ROIs were

Table 1
Tissue distribution of radioactivity in mice after intravenous injection of *O*-[^{11}C]methyl-L-tyrosine

	% Injection dose/g tissue[a]					
	1 min	5 min	15 min	30 min	60 min	90 min
Blood	3.12±0.22	2.33±0.21	2.17±0.03	1.85±0.09	1.57±0.18	1.33±0.09
Brain	0.36±0.08	0.71±0.06	0.87±0.03	1.01±0.10	0.89±0.08	0.86±0.10
Heart	3.31±0.30	2.13±0.20	1.94±0.03	1.71±.09	1.54±0.15	1.34±0.09
Lung	2.49±0.31	1.98±0.16	1.85±0.15	1.56±0.13	1.38±0.19	1.24±0.08
Liver	2.77±0.23	1.95±015	1.80±0.07	1.64±0.07	1.41±0.15	1.22±0.11
Spleen	1.78±0.54	2.36±0.40	2.00±0.05	1.91±0.19	1.54±0.12	1.33±0.09
Pancreas	8.74±2.45	11.94±1.02	8.21±1.01	8.60±0.72	8.79±1.98	10.54±1.56
Stomach	1.13±0.13	1.22±0.39	1.02±0.21	1.43±0.22	1.39±0.80	1.05±0.18
Small intestine	2.33±0.26	2.12±0.15	1.71±0.17	1.81±0.23	1.56±0.31	1.69±0.18
Large intestine	1.02±0.13	0.92±0.07	1.02±0.06	0.81±0.10	0.62±0.03	0.67±0.09
Kidney	3.32±0.41	2.66±0.31	2.68±0.31	2.46±0.74	2.33±0.53	2.34±0.64
Testis	0.57±0.08	1.03±0.19	1.65±0.14	1.45±0.41	1.25±0.18	1.20±0.16
Bone	1.40±0.27	1.44±0.15	1.46±0.08	1.20±0.17	1.01±0.17	0.84±0.09
Muscle	1.68±0.11	1.98±0.20	1.91±0.08	1.49±0.24	1.48±0.16	1.27±0.06

[a] Mean±S.D. (n=4).

expressed as a SUV [(regional activity/ml volume)/(injected activity/g body weight)].

2.8. Clinical study

Two male volunteers (21 years old, 62.5 kg; and 53 years old, 61.3 kg), a female volunteer (21 years old, 48.2 kg) and a male patient with recurrent oligodendroglioma (47 years old, 93.0 kg) participated in the present study, and a written informed consent was obtained from them. Three volunteers were healthy according to the history and clinical investigations. The PET camera used was SET-2400W (Shimadzu, Kyoto, Japan), which has an axial field-of-view of 20 cm and acquires 63 slices at a center-to-center interval of 3.125 mm [17].

In healthy subjects, *O*-[^{11}C]methyl-L-tyrosine (700–770 MBq/13–27 nmol) was injected intravenously after transmission scanning with a rotating [^{68}Ge]/[^{68}Ga] line source to correct for attenuation. In the subjects 1 and 2, the PET scans were performed in the head and in the abdominal region including the liver and pancreas, respectively, for 30 min (30 s×5 frames, 1 min×5 frames, 1.5 min×1 frame, 2.5 min×4 frames and 5 min×2 frames) in 2D mode. Then, from 50 to 78 min after the tracer injection, the whole-body scan spanning from the thighs to neck was performed in 2D mode (four overlapping bed positions, 7-min emission time per position, with simultaneous attenuation correction). During the first 30-min dynamic scans, arterial blood was taken at 10, 20, 30, 40, 50, 60, 70, 80, 90, 100, 110 and 120 s, and 2.5, 3, 5, 7.5, 10, 15, 20 and 30 min, and the radioactivity levels in whole blood and plasma were expressed as SUV. Metabolites in the plasma sampled at 3, 10, 20 and 30 min were analyzed by HPLC analysis: column, Nova-pak C18 column (8.0 mm inner diameter×100 mm length) equipped with an RCM 8×10 compression module (Waters, Milford, MA); mobile phase, CH_3CN/50 mM CH_3CO_2H/50 mM CH_3CO_2Na (5:47.5:47.5, v/v/v); flow rate, 2 ml/min; a radioactivity detector, FLO-ONE/Beta A200 (Packard, Meriden, CT); and retention time, 5.1 min as previously described [12]. In subject 3, 10 min after intravenous injection of the tracer, a whole-body scan spanning from the thighs to head was similarly performed in five overlapping bed positions with a 7-min scan per position, and

Table 2
Organ distribution of radioactivity in mice after intravenous injection of *O*-[^{11}C]methyl-L-tyrosine

	% Injection dose/organ[a]					
	1 min	5 min	15 min	30 min	60 min	90 min
Brain	0.16±0.04	0.29±0.03	0.42±0.05	0.47±0.04	0.44±0.04	0.39±0.04
Heart	0.51±0.05	0.37±0.04	0.30±0.01	0.26±0.01	0.21±0.02	0.19±0.01
Lung	0.51±0.04	0.42±0.07	0.38±0.02	0.35±0.03	0.30±0.06	0.25±0.03
Liver	4.61±0.35	3.36±0.59	3.34±0.07	3.06±0.41	2.32±0.19	1.91±0.42
Spleen	0.17±0.05	0.27±0.07	0.23±0.04	0.21±0.07	0.20±0.03	0.15±0.02
Pancreas	1.83±0.54	2.70±0.46	2.22±0.21	1.88±0.39	1.95±0.47	2.28±0.35
Stomach	0.76±0.16	0.68±0.02	0.62±0.11	0.57±0.20	0.75±0.41	0.48±0.08
Small Intestine	4.75±0.37	4.33±0.15	3.65±0.26	3.78±0.40	3.28±0.32	3.07±0.46
Large Intestine	1.05±0.23	0.84±0.16	1.00±0.07	0.75±0.08	0.59±0.08	0.51±0.07
Kidney	1.58±0.40	1.51±0.24	1.43±0.28	1.45±0.44	1.25±0.35	1.31±0.43
Testis	0.12±0.01	0.24±0.03	0.26±0.02	0.37±0.12	0.30±0.10	0.29±0.03
Bladder	0.08±0.08	0.10±0.03	0.23±0.07	0.21±0.15	0.16±0.08	0.31±0.20
Urine	0.09±0.07	1.15±0.43	4.05±1.40	8.64±2.41	13.52±2.89	14.50±2.97

[a] Mean±S.D. (n=4).

Table 3
Absorbed dose of *O*-[^{11}C]methyl-L-tyrosine for human adults estimated from mouse data

	μGy/MBq		μGy/MBq
Brain	0.64	Upper large intestine wall	4.98
Thyroid	3.62	Lower large intestine wall	4.62
Thymus	4.07	Adrenals	6.17
Breast	3.54	Kidneys	4.92
Heart	2.19	Testis	3.30
Lungs	4.66	Ovaries	15.20
Livers	2.09	Uterus	5.09
Pancreas	2.25	Bladder	3.47
Spleen	3.38	Bone surfaces	0.54
Stomach wall	3.35	Red marrow	2.42
Small intestine wall	5.38	Bones	1.88
Total body	4.54 μSv/MBq		

then 50 min after the tracer injection, a second whole-body scan was performed.

From all the three subjects, urine was recovered 100 min postinjection of the tracer and the radioactivity was measured, and the unaltered *O*-[^{11}C]methyl-L-tyrosine was analyzed by HPLC as described above.

A patient with recurrent oligodendroglioma was intravenously given *O*-[^{11}C]methyl-L-tyrosine (403 MBq/10.7 nmol) following the transmission scanning, and a 60-min PET scan was performed in the head region in three-dimensional (3D) mode without arterial blood sampling.

The brain tomographic images were reconstructed using a Fourier rebinning algorithm [18] and a filtered backprojection method with Butterworth filter (cutoff frequency 1.25 cycle/cm and order 2). The data were collected in a 128×128×63 matrix, and the voxel size was 2×2×3.125 mm. Voxel counts were calibrated to activity concentration (Bq/ml). ROIs were placed on the temporal cortex and cerebellum in the first volunteer, on the heart, lung, liver, pancreas, spleen, kidney and muscle in the second volunteer and on the temporal cortex and two tumor regions in the patient with recurrent oligodendroglioma. Time–activity curves of these ROIs were calculated as an SUV. The body tomographic images were reconstructed using an ordered subsets expectation maximization (OSEM) method (subsets 16, iteration 2). The data were collected in 128×128×124 and 128×128×155 matrixes in four and five overlapping bed positions, respectively, and the voxel size was 4×4×6.25 mm.

3. Results

3.1. Radiation dosimetry

The tissue distribution of the radioactivity after injection of *O*-[^{11}C]methyl-L-tyrosine into mice is summarized in Tables 1 and 2. The pancreas retained the high uptake (%ID/g) over 90 min. The brain uptake was low but increased for the first 30 min, and then slightly decreased. The levels of radioactivity in all other tissues gradually decreased as observed in that in blood. After 30 min of the tracer injection, the levels in only the pancreas and kidneys were higher than in the blood level. Approximately 15% of the total injected radioactivity was excreted into urine over 90 min. From these data, the radiation-absorbed doses were estimated (Table 3). The radiation-absorbed doses were slightly higher in the ovaries than in the other organs studied, and were very low in the brain and bone surfaces.

3.2. Acute toxicity

Acute toxicity was evaluated after an intravenous administration of *O*-methyl-L-tyrosine at a dose of 2.41 mg/kg, and after an intravenous injection of three lots of *O*-[^{11}C]methyl-L-tyrosine preparations at a dose range of 1.43–5.71 μg/kg. No mortality was found in the rats. All groups of rats showed normal gain in the body weight compared with the control animals, and no clinical signs were observed over a 15-day period. Also, no abnormality was found in their postmortem macroscopic examination.

Table 4
Tissue distribution of radioactivity in rats bearing inflammation and AH109A tumor 30 min after intravenous injection of *O*-[^{11}C]methyl-L-tyrosine

		Inflammatory tissue	AH109A	Muscle	Blood
O-[^{11}C]methyl-L-tyrosine[a]	Uptake (%ID/g)	0.42±0.08	1.75±0.13	0.49±0.03	0.49±0.02
	Inflammation/tissue		0.24	0.85	0.85
	AH109A/tissue	4.2		3.6	3.5
L-[*methyl*-^{11}C]methionine[b]	Uptake (%ID/g)	0.25±0.08	1.61±0.30	0.38±0.03	0.21±0.03
	Inflammation/tissue		0.15	0.66	1.2
	AH109A/tissue	6.4		4.2	7.7
[^{3}H]DG[c]	Uptake (%ID/g)	0.62±0.10	2.01±0.28	0.16±0.07	0.12±0.05
	Inflammation/tissue		0.32	4.4	5.5
	AH109A/tissue	3.4		13.8	17.7

[a] Present study. Mean±S.D. (n=7).

[b] Uptake was measured 20 min postinjection of L-[*methyl*-^{11}C]methionine [3] and corrected for a percentage of the injected dose per gram of tissue (%ID/g). AH109A ascitic hepatoma was inoculated on the back of Donryu rats as described in the present study, and inflammation was induced by croton oil on the back. Mean±S.D. (n=10).

[c] Data were obtained 60 min postinjection of 2-deoxy-D-[2.6-^{3}H]glucose ([^{3}H]DG) in rats prepared by the same way in the present study (unpublished data). Mean±S.D. (n=5).

3.3. Mutagenicity

When a bacterial reverse mutation test was conducted on *S. typhimurium* mutation test, no mutagenic activity was observed for *O*-methyl-L-tyrosine.

3.4. Uptake study in a rat inflammation model

The uptake of *O*-[^{11}C]methyl-L-tyrosine in inflammatory tissue and AH109A is summarized in Table 4. The radioactivity level in inflammatory tissue was slightly lower than those in blood and muscle and much lower than that in AH109A.

3.5. Monkey study

Fig. 2 shows the time sequential PET images of the brain and whole-body in each of the two monkeys after injection of *O*-[^{11}C]methyl-L-tyrosine. All physiological parameters measured were retained normal during the PET experiment in the dynamic whole-body imaging. The time–activity curves of several tissues are shown in Fig. 3. The tracer was taken at similar levels in the heart, liver, pancreas and kidney followed by a rapid clearance for the first 15 min. The uptake in the brain and muscle was low and slightly increased for the first 15–30 min. The uptake in the lung was very low over 90 min. After 20 min, the radioactivity levels investigated remained constant. Radioactivity in blood and plasma rapidly decreased for the first 15 min and then remained constant. The levels were comparable with those in the heart, liver and pancreas and were higher than those in the brain, lung and muscle. In the plasma, incorporation of the radioactivity into the protein fraction was negligible for 90 min, and percentages of the unchanged form of *O*-[^{11}C]methyl-L-tyrosine slightly decreased with time: 85%, 86%, 83%, 84% and 83%, at 5, 15, 30, 60 and 90 min, respectively.

3.6. Clinical study

In the early tomographic images of the abdominal region that was acquired 0–5 min postinjection of *O*-[^{11}C]methyl-L-tyrosine (Fig. 4A), the heart, liver, pancreas, spleen and kidney were visualized, while they were obscured in the late images (20–30 min postinjection of the tracer) with the exception of hot spots reflecting the renal pelvis. Thus, the radioactivity levels of these organs rapidly decreased for the first 15 min followed by a gradual decrease (Fig. 5). In the brain (images in the healthy subject not shown) and muscle, the uptake was low and slightly increased for 30 min. Lung uptake was very low. In the whole-body images acquired for 10–45 min postinjection (Fig. 4B), the radioactivity levels of these organs were low and only the bladder showed a high spot. In the later whole-body images that were obtained 50–85 min in the three subjects (images not shown), the relative contrast was comparable with the images obtained 10–45 min except for the increasing radioactivity in the bladder.

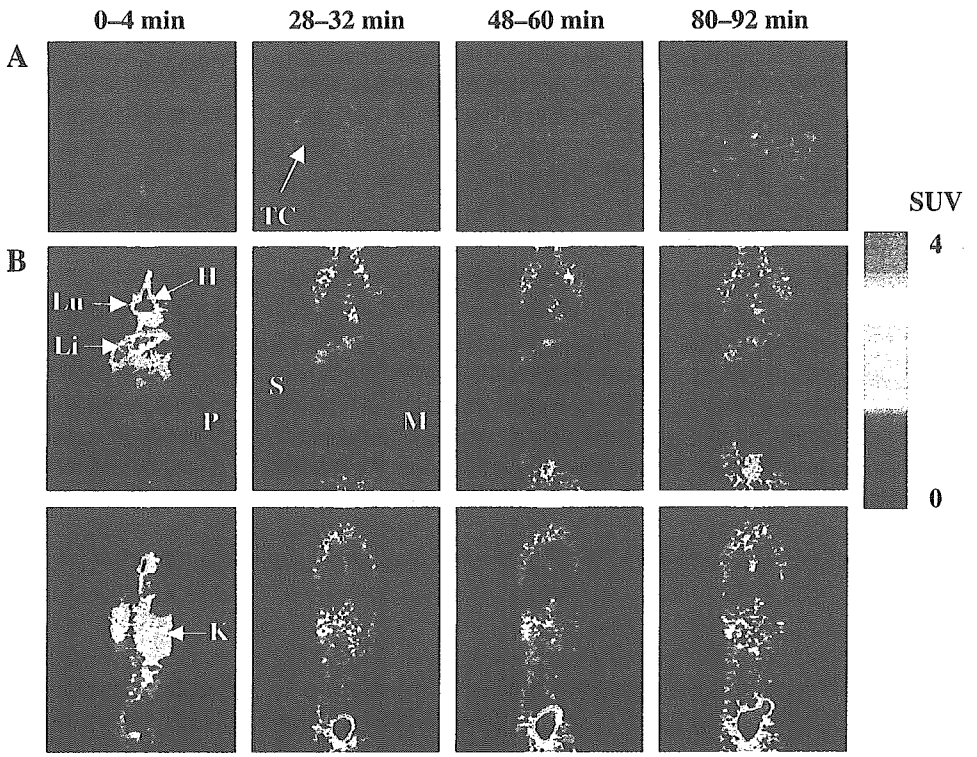

Fig. 2. PET images with *O*-[^{11}C]methyl-L-tyrosine in monkeys. Brain images (A) and whole body images (B) were obtained from different monkeys. The images shown were acquired for 0–4, 28–32, 48–60 and 80–92 min in four overlapping bed positions from the neck to thighs. The range of radioactivity level was 0–4 SUV. H, heart; K, kidney; Li, liver; Lu, lung; M, muscle; P, pancreas; and TC, temporal cortex.

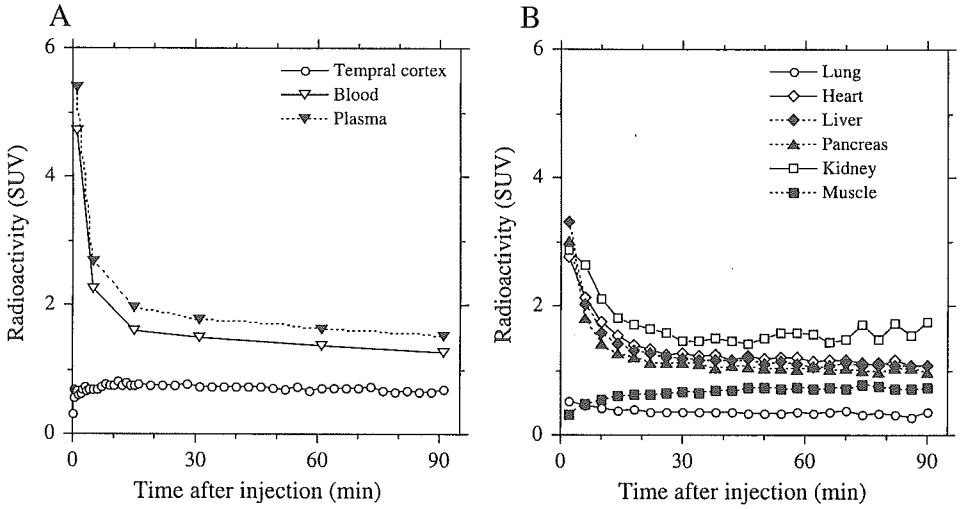

Fig. 3. Time–activity curves of *O*-[^{11}C]methyl-L-tyrosine in monkeys. The radioactivity was measured in the regions of interest indicated in Fig. 2. A, Monkey 1 presented in Fig. 2A; and B, monkey 2 in Fig. 2B.

Radioactivity in blood and plasma rapidly decreased for the first 5 min followed by a gradual decrease. Thirty minutes later postinjection, the levels were in blood and plasma were comparable with those in the brain and muscle. In the plasma, the radioactivity was negligible in the protein fraction for 30 min, and percentages of the unaltered *O*-[^{11}C]methyl-L-tyrosine slightly decreased: 98%, 98%, 98% and 92%, at 3, 10, 20 and 30 min, respectively (n=2). At 100 min after the tracer injection, 6.0% (range, 4.4–8.3%; n=3) of the radioactivity was excreted into urine and percentages of the unaltered *O*-[^{11}C]methyl-L-tyrosine was 68% (range, 55.3–81.4%; n=3).

Fig. 4C represents the tomographic brain images of the patient with recurrent oligodendroglioma after injection of *O*-[^{11}C]methyl-L-tyrosine. The radioactivity levels in both tumor and brain increased for the first 15 min and then

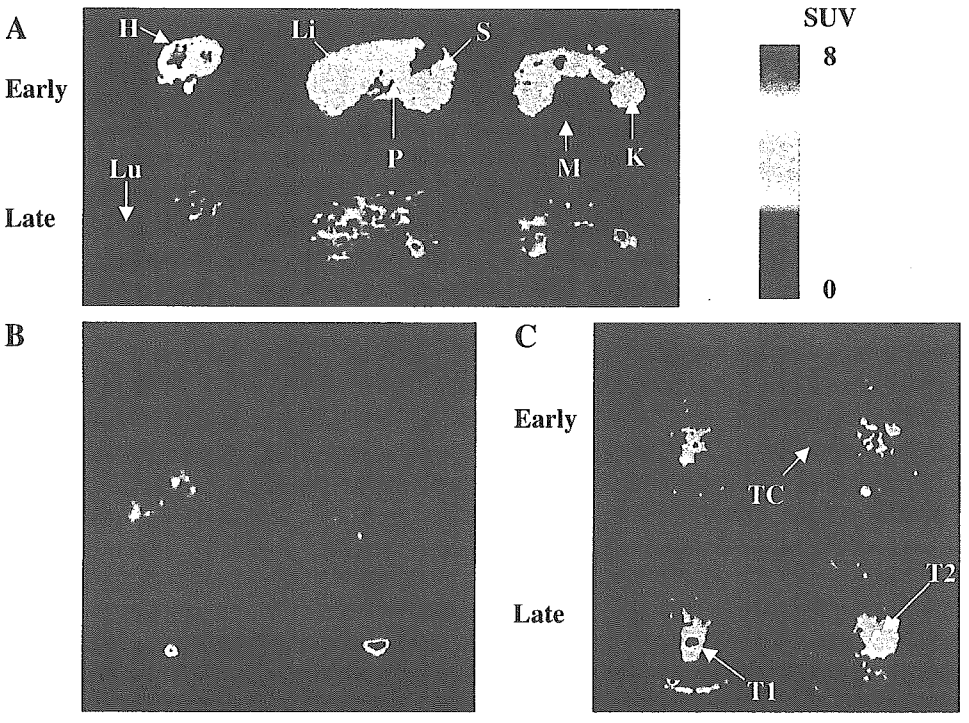

Fig. 4. PET images with *O*-[^{11}C]methyl-L-tyrosine in human subjects. Tomographic images of the abdominal region (A) and whole-body images (B) were obtained from healthy subjects 2 and 3, respectively, and brain images (C) were obtained from a patient with recurrent oligodendroglioma. The early and late images in A and C were acquired for 0–5 and 20–30 min, respectively, after tracer injection, and the whole body images were acquired for 10–45 min in five overlapping bed positions from the thighs to head. The range of radioactivity level was 0–8 SUV. H, heart; K, kidney; Li, liver; Lu, lung; M, muscle; P, pancreas; S, spleen; TC, temporal cortex; T1, tumor region 1; and T2, tumor region 2.

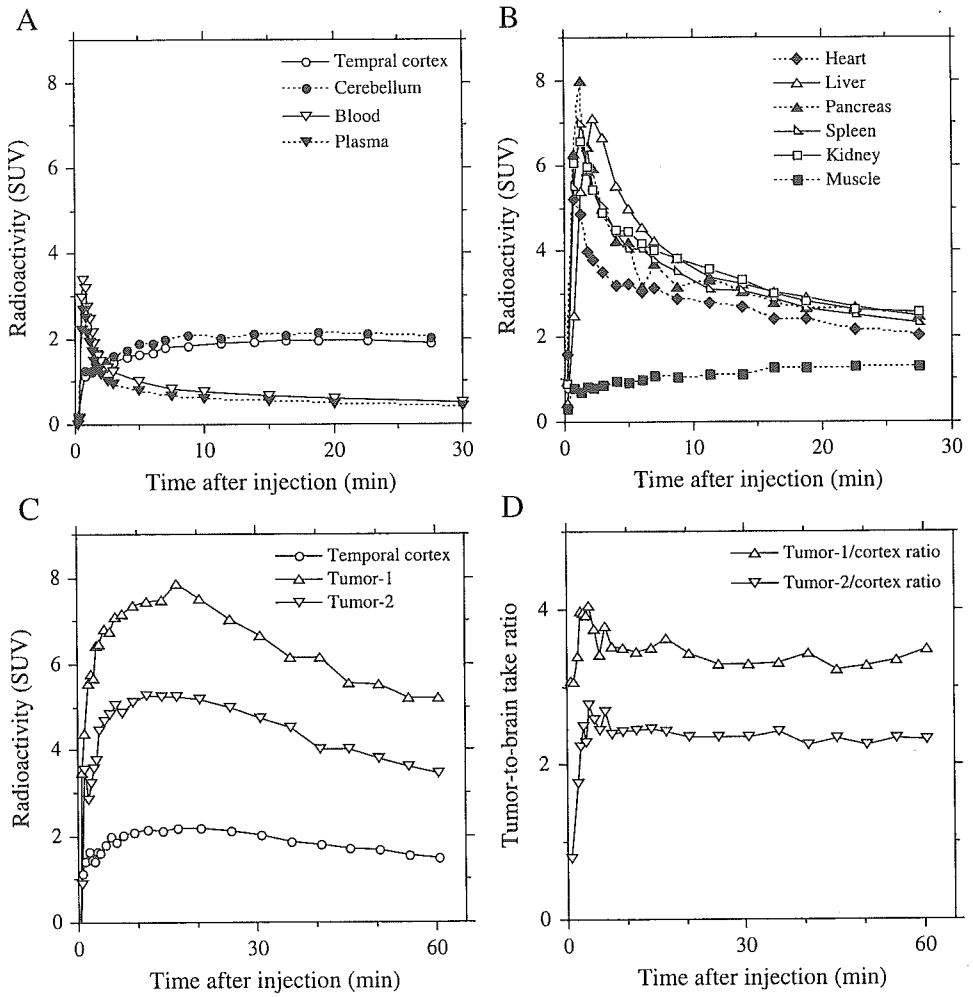

Fig. 5. Time–activity curves of *O*-[^{11}C]methyl-L-tyrosine in human subjects (A–C) and uptake ratios of tumor to brain in a patient with recurrent oligodendroglioma (D). The radioactivity was measured in the ROIs indicated in Fig. 4. Two regions of tumors and temporal cortex were representatively selected (C). A, Healthy subject 1 (images not shown); B, healthy subject 3 (Fig. 4B); and C, patient with tumor.

gradually deceased (Fig. 5C). The uptake ratios of tumor to normal brain were constant 10 min after the tracer injection (Fig. 5D).

4. Discussion

In the previous study using a tumor bearing rat model, we have demonstrated that *O*-[^{11}C]methyl-L-tyrosine has the potential for tumor imaging in terms of the amino acid transport [12]. In the present study, we investigated suitability of *O*-[^{11}C]methyl-L-tyrosine in clinical use. The radiation-absorbed dose was low enough for clinical use. Although *O*-methyl-L-tyrosine is commercially available, its toxicological data were limited. Thus, we confirmed no abnormality in rats in the acute toxicity test and no mutagenicity of *O*-methyl-L-tyrosine.

In PET studies of monkeys and healthy subjects, we found that tracer kinetics was slightly different between rodents and primates. Dynamic whole-body imaging of a monkey using the multiple-bed position technique showed low uptake of *O*-[^{11}C]methyl-L-tyrosine in the pancreas that was comparable to the uptake in the liver or heart in spite of the highest uptake in the pancreas among the organs in rats [12] and mice (Table 1). Similarly, low uptake of *O*-[^{11}C]methyl-L-tyrosine in the pancreas was also confirmed in humans. Thus, in the pancreas, high uptake in rodents but low uptake in humans appears to be common in the artificial amino acids such as *O*-[^{18}F]fluoroethyl-L-tyrosine [6], 3-[^{18}F]fluoro-α-methyl-L-tyrosine [19] and 4-[^{18}F]fluoro-L-proline [20,21]. In contrast to these artificial amino acids, high uptake in the pancreas and liver of humans was observed for an artificial amino acid 2-[^{18}F]fluoro-L-tyrosine [22] and natural amino acids like L-[*methyl*-^{11}C]methionine [1] and L-[1-^{11}C]tyrosine [5], which were incorporated into protein synthesis in experimental animals [23–25]. These findings demonstrate a potential benefit of the artificial amino acids like *O*-[^{11}C]methyl-L-tyrosine for tumor imaging in the whole-body compared with natural amino acids as discussed below.

The other different characteristic of *O*-[^{11}C]methyl-L-tyrosine between rodents and primates was found in

peripheral metabolism, although incorporation of the radioactivity into a protein fraction was not found in plasma and AH109A tumor of rats [12] and in plasma of monkeys and humans (present study). On the other hand, in rats, we did not find any acid-soluble metabolites of *O*-[^{11}C]methyl-L-tyrosine in plasma and tumor tissue for 30 min, while small amounts of labeled metabolites were found in plasma of primates: percentages of unaltered *O*-[^{11}C]methyl-L-tyrosine were 83% and 92% in a monkey and humans (n=2), respectively, 30 min postinjection. The degradation of *O*-[^{11}C]methyl-L-tyrosine in humans was very slow, but in urine recovered 100 min postinjection, 32% (n=3) of the radioactivity was detected as labeled metabolites of *O*-[^{11}C]methyl-L-tyrosine. A similar discrepancy between rodents and humans were also reported for *O*-[^{18}F]fluoroethyl-L-tyrosine: no metabolites in mice [6] but 7% and 39% of metabolites in plasma at 30 min and in urine at 150 min postinjection, respectively [26].

As far as tumor diagnosis, a preliminary patient study clearly visualized recurrent oligodendroglioma. Because the tumor-to-brain uptake ratios were constant after 10 min postinjection, the static PET imaging for tumor diagnosis of the brain could be done within 30 min after the tracer injection. On the other hand, from the viewpoint of kinetic analysis to evaluate amino acid transport in tumors, a longer PET scan more than 30 min may be required to obtain stable kinetic parameters, when taking into account the time–activity curves of tumor and brain tissues: an increasing radioactivity for the first 15 min followed by a gradual decrease (Fig. 5C). Also, the metabolite analysis of plasma may be necessary.

Whole-body imaging of monkeys and healthy subjects clearly demonstrated applicability of the *O*-[^{11}C]methyl-L-tyrosine PET for tumor diagnosis in the whole-body except for the urinary tract. The relative whole-body distribution of the radioactivity in a healthy subject was not different between the early images (10–45 min postinjection) and late images (50–85 min) except for an increasing radioactivity in the bladder in addition to much lower signal in the late images. It should be taken into consideration that the muscular uptake slightly increased with time and that the blood level was relatively high. Thus, the whole-body imaging could be done within 60 min starting the scan 10–20 min postinjection. The early time frame may be preferable because of a relatively low radioactivity level in the bladder. The whole-body images shown in Fig. 4B are comparable to those obtained by *O*-[^{18}F]fluoroethyl-L-tyrosine PET scan starting about 70 min postinjection where the urinary tract was clearly visualized [6,26]. In the case of whole-body imaging with 3-[^{18}F]fluoro-α-methyl-L-tyrosine PET 40 min later of the tracer injection, the kidney was much more clearly visualized [19]. In spite of low uptake in the normal liver and pancreas, 4-[^{18}F]fluoro-L-proline appears not to be a promising PET tracer in oncology [21]. When compared the brain-to-blood ratios of *O*-[^{11}C]methyl-L-tyrosine with those of ^{18}F-labeled artificial amino acids, blood clearance of *O*-[^{11}C]methyl-L-tyrosine seems faster than that of *O*-[^{18}F]fluoroethyl-L-tyrosine [6] or 4-[^{18}F]fluoro-L-proline [27] and is comparable to that of 3-[^{18}F]fluoro-α-methyl-L-tyrosine [28].

The possible advantage of the radiolabeled amino acids is presently for differential diagnosis of tumors from inflammation, compared to [^{18}F]FDG that accumulates inflammatory tissues [1]. In animal studies, low uptake in the inflammatory tissues was demonstrated for L-[*methyl*-^{11}C]-methionine [3], *O*-[^{18}F]fluoroethyl-L-tyrosine [29], *O*-[^{18}F]fluoropropyl-L-tyrosine [30] and 3-[^{123}I]iodo-α-methyl-L-tyrosine [31]. In the present study, we also confirmed the low accumulation of *O*-[^{11}C]methyl-L-tyrosine in an acute inflammation model [13]. When compared the uptake of *O*-[^{11}C]methyl-L-tyrosine, L-[*methyl*-^{11}C]methionine [3] and 2-deoxy-D-[2,6-^{3}H]glucose (a ^{3}H-labeled counterpart of [^{18}F]FDG) (unpublished data) in the inflammation and AH109A hepatoma (Table 4), the uptake ratios of inflammation to muscle and inflammation to blood for 2-deoxy-D-[2,6-^{3}H]glucose were much larger than those for radiolabeled amino acids. Two radiolabeled amino acids have the comparable potential for the differential diagnosis between tumor and inflammation. However, it is noticed that the contrast for tumor imaging, that is, the uptake ratios of tumor to muscle and tumor to blood, is most preferable for [^{18}F]FDG followed by L-[*methyl*-^{11}C]methionine and *O*-[^{11}C]methyl-L-tyrosine. These differences between [^{18}F]FDG and *O*-[^{11}C]methyl-L-tyrosine are mainly due to a rapid clearance of [^{18}F]FDG and a slow clearance of *O*-[^{11}C]methyl-L-tyrosine in the muscle and blood.

In conclusion, *O*-[^{11}C]methyl-L-tyrosine is suitable for clinical use and the *O*-[^{11}C]methyl-L-tyrosine PET has the potential for tumor imaging in the whole-body except for the urinary tract and bladder.

Acknowledgments

This work was supported by Grants-in-Aid for Scientific Research (C) No. 13470177 of Japan Society for the Promotion of Science (to R.I.) and for Research and Development of Technology for Measuring Vital Function Merged with Optical Technology, Research and Development Project Aimed at Economic Revitalization (to H.T.) and Budget for Nuclear Research of the Ministry of Education, Culture, Sports, Science and Technology (to K.K.). The authors thank Ms. Miyoko Ando for her care of the subject in PET measurement.

References

[1] Kubota K. From tumor biology to clinical PET: a review of positron emission tomography (PET) in oncology. Ann Nucl Med 2001; 15:471–86.

[2] Kubota R, Yamada S, Kubota K, Ishiwata K, Tamahashi N, Ido T. Intratumoral distribution of fluorine-18-fluorodeoxyglucose in vivo: high accumulation in macrophages and granulation tissues studied by microautoradiography. J Nucl Med 1992;33:1972–80.

[3] Kubota K, Matsuzawa T, Fujiwara T, Sato T, Tada M, Ido T, et al. Differential diagnosis of AH109A tumor and inflammation by radioscintigraphy with L-[*methyl*-^{11}C]methionine. Jpn J Cancer Res 1989;80:778–82.

[4] Vaalburg W, Coenen HH, Crouzel C, Elsinga PH, Långström B, Lemaire C, et al. Amino acids for the measurement of protein synthesis in vivo by PET. Nucl Med Biol 1992;19:227–37.

[5] Jager PL, Vaalburg W, Pruim J, de Vries EGE, Langan KJ, Piers A. Radiolabeled amino acids: basic aspects and clinical application in oncology. J Nucl Med 2001;42:432–45.

[6] Wester HJ, Herz M, Weber W, Heiss P, Senekowitsch-Schmidtke R, Schwaiger M, et al. Synthesis and radiopharmacology of *O*-(2-[^{18}F]fluoroethyl)-L-tyrosine for tumor imaging. J Nucl Med 1999; 40:205–12.

[7] Lemaire C, Guillaume M, Christiaens L, Palmer AJ, Cantineau R. A new route for the synthesis of [^{18}F]fluoroaromatic substituted amino acids: no carrier added L-*p*-[^{18}F]fluorophenylalanine. Int J Radiat Appl 1987;38:1033–8.

[8] Hamacher K. Synthesis of n.c.a. *cis*- and *trans*-4-[^{18}F]fluoro-L-proline, radiotracers for PET-investigation of disordered matrix protein synthesis. J Label Compd Radiopharm 1999;42:1135–44.

[9] Shoup TM, Olson J, Hoffman JM, Votaw J, Eshima D, Eshima L, et al. Synthesis and evaluation of [^{18}F]1-amino-3-fluorocyclobutane-1-carboxylic acid to image brain tumors. J Nucl Med 1999;40:331–8.

[10] Tang G, Tang X, Wang M, Luo L, Gan M. Fully automated synthesis of *O*-(3-[^{18}F]fluoropropyl)-L-tyrosine by direct nucleophilic exchange on a quaternary 4-aminopyridinium resin. Appl Radiat Isot 2003; 58:685–9.

[11] Iwata R, Furumoto S, Pascali C, Bogni A, Ishiwata K. Radiosynthesis of *O*-[^{11}C]methyl-L-tyrosine and *O*-[^{18}F]fluoromethyl-L-tyrosine as potential PET tracers for imaging amino acid transport. J Label Compd Radiopharm 2002;46:555–66.

[12] Ishiwata K, Kawamura K, Wang WF, Furumoto S, Kubota K, Pascali C, et al. Evaluation of *O*-[^{11}C]methyl-L-tyrosine and *O*-[^{18}F]fluoromethyl-L-tyrosine as tumor imaging tracers by PET. Nucl Med Biol 1993;31:191–8.

[13] Yamada S, Kubota K, Kubota R, Ido T, Tamahashi N. High accumulation of fluorine-18-fluorodeoxyglucose in turpentine-induced inflammatory tissue. J Nucl Med 1995;36:1301–6.

[14] Mejia AA, Nakamura T, Itoh M, Hatazawa J, Ishiwata K, Ido T, et al. Absorbed dose estimates in positron emission tomography studies based on the administration of ^{18}F-labeled radiopharmaceuticals. J Radiat Res 1991;32:243–61.

[15] Watanabe M, Okada H, Shimizu K, Omura T, Yoshikawa E, Kosugi T, et al. A high resolution animal PET scanner using compact PS-PMT detectors. IEEE Trans Nucl Sci 1997;44:1277–82.

[16] Tsukada H, Nishiyama S, Kakiuchi T, Ohba H, Sato K, Harada N. Is synaptic dopamine concentration the exclusive factor which alters the in vivo binding of [^{11}C]raclopride?: PET studies combined with microdialysis in conscious monkeys. Brain Res 1999;841:160–9.

[17] Fujiwara T, Watanuki S, Yamamoto S, Miyake M, Seo S, Itoh M, et al. Performance evaluation of a large axial field-of-view PET scanner: SET-2400W. Ann Nucl Med 1997;11:307–13.

[18] Defrise M, Kinahan PE, Townsend DW, Michel C, Sibomana M, Newport DF. Exact and approximate rebinning algorithms for 3-D PET data. IEEE Trans Med Imaging 1997;16:145–58.

[19] Inoue T, Koyama K, Oriuchi N, Alyafei S, Yuan Z, Suzuki H, et al. Detection of malignant tumors: whole-body PET with fluorine 18 α-methyl tyrosine versus FDG — preliminary study. Radiology 2001; 220:54–62.

[20] Börner AR, Langen KJ, Herzog H, Hamacher K, Müller-Mattheis V, Schmitz T, et al. Whole-body kinetics and dosimetry of *cis*-4-[^{18}F]fluoro-L-proline. Nucl Med Biol 2001;28:287–92.

[21] Langen KJ, Börner AR, Müller-Mattheis V, Hamacher K, Herzog H, Ackermann R, et al. Uptake of *cis*-4-[^{18}F]fluoro-L-proline in urologic tumors. J Nucl Med 2001;42:752–4.

[22] Hustinx R, Lemaire C, Jerusalem G, Moreau P, Cataldo D, Duysinx B, et al. Whole-body tumor imaging using PET and 2-^{18}F-fluoro-L-tyrosine: preliminary evaluation and comparison with ^{18}F-FDG. J Nucl Med 2003;44:533–9.

[23] Ishiwata K, Kubota K, Murakami M, Kubota R, Sasaki T, Ishii S, et al. Re-evaluation of amino acid-PET studies: can the protein synthesis rates in brain and tumor tissues be measured in vivo? J Nucl Med 1993;34:1936–43.

[24] Coenen HH, Kling P, Stocklin G. Cerebral metabolism of L-[2-^{18}F]fluorotyrosine, a new PET tracer of protein synthesis. J Nucl Med 1989;30:1367–72.

[25] Ishiwata K, Vaalburg W, Elsinga PH, Paans AMJ, Woldring MG. Metabolic studies with L-[1-^{14}C]tyrosine for the investigation of a kinetic model to measure protein synthesis rates with PET. J Nucl Med 1988;29:524–9.

[26] Pauleit D, Floeth F, Herzog H, Hamacher K, Tellmann L, Muller HW, et al. Whole-body distribution and dosimetry of *O*-(2-[^{18}F]fluoroethyl)-L-tyrosine. Eur J Nucl Med Mol Imaging 2003;30:519–24.

[27] Langen KJ, Jarosch M, Hamacher K, Mühlensiepen H, Weber F, Floeth F, et al. Imaging of gliomas with *cis*-4-[^{18}F]fluoro-L-proline. Nucl Med Biol 2004;31:67–75.

[28] Inoue T, Shibasaki T, Oriuchi N, Aoyagi K, Tomiyoshi K, Amano S, et al. ^{18}F α-methyl tyrosine PET studies in patients with brain tumors. J Nucl Med 1999;40:399–405.

[29] Rau FC, Weber WA, Wester HJ, Herz M, Becker I, Kruger A, et al. *O*-(2-[^{18}F]Fluoroethyl)-L-tyrosine (FET): a tracer for differentiation of tumour from inflammation in murine lymph nodes. Eur J Nucl Med Mol Imaging 2002;29:1039–46.

[30] Tang G, Wang M, Tang X, Luo L, Gan M. Synthesis and evaluation of *O*-(3-[^{18}F]fluoropropyl)-L-tyrosine as an oncologic PET tracer. Nucl Med Biol 2003;30:733–9.

[31] Kuwert T, Morgenroth C, Woesler B, Matheja P, Palkovic S, Vollet B, et al. Uptake of iodine-123-alpha-methyl tyrosine by gliomas and non-neoplastic brain lesions. Eur J Nucl Med 1996;23:1345–53.

ELSEVIER

NeuroImage

www.elsevier.com/locate/ynimg
NeuroImage 26 (2005) 885–890

Omission of serial arterial blood sampling in neuroreceptor imaging with independent component analysis

Mika Naganawa,[a] Yuichi Kimura,[b,*] Tadashi Nariai,[c] Kenji Ishii,[b] Keiichi Oda,[b] Yoshitsugu Manabe,[a] Kunihiro Chihara,[a] and Kiichi Ishiwata[b]

[a]*Department of Information Processing, Graduate School of Information Science, Nara Institute of Science and Technology, Nara, Japan*
[b]*Positron Medical Center, Tokyo Metropolitan Institute of Gerontology, 1-1, Naka, Itabashi, Tokyo, 173-0022, Japan*
[c]*Department of Neurosurgery, Tokyo Medical and Dental University, Tokyo, Japan*

Received 4 December 2004; revised 9 February 2005; accepted 17 February 2005
Available online 1 April 2005

We have previously proposed a statistical method for extracting a plasma time–activity curve (pTAC) from dynamic PET images, named EPICA, for kinetic analysis of cerebral glucose metabolism. We assumed that the dynamic PET images consist of a blood-related component and a tissue-related component which are spatially independent in a statistical sense. The aim of this study is to investigate the utility of EPICA in imaging total distribution volume (DVt) and binding potential (BP) with Logan plots in a neuroreceptor mapping study. We applied EPICA to dynamic [^{11}C]MPDX PET images in 25 subjects, including healthy subjects and patients with brain diseases, and validated the estimated pTACs. [^{11}C]MPDX is a newly developed radiopharmaceutical for mapping cerebral adenosine A_1 receptors. EPICA successfully extracted pTAC for all 25 subjects. Parametric images of DVts were estimated by applying Logan plots with the EPICA-estimated pTAC and then used to define a reference region. The BPs estimated using EPICA were evaluated in 18 subjects by ROI-based comparison with those obtained using the nonlinear least squares method (NLSM). The calculated BPs were identical to the estimates using NLSM in each subject. We conclude that EPICA is a promising technique that generates parametric images of DVt and BP in neuroreceptor mapping without requiring arterial blood sampling.

Keywords: Arterial blood sampling; Adenosine A_1 receptor; Independent component analysis

Introduction

Positron emission tomography (PET) is a nuclear medicine-based technique that provides tomographic images of the distribution of positron-emitting radiopharmaceuticals. Quantitative analysis of the measured PET data, known as kinetic analysis, investigates the relationship of the histories of the radioactivity concentrations in the arterial blood and target organs. Kinetic analysis provides quantitative and useful parameters such as cerebral metabolic rate of glucose and binding potential. For example, Logan plots (Logan, 2000; Logan et al., 1990) are a robust estimation technique for the total distribution volume (DVt) of neuroreceptor radioligands that have reversible binding kinetics. DVt is the sum of the free/non-specific distribution volume and the specific distribution volume.

To perform Logan plots, the time courses of the radioactivity in plasma from arterial blood (plasma time–activity curve; pTAC) and in the target tissue (tissue time–activity curve; tTAC) are required. pTAC is usually measured by serial arterial blood sampling via a catheter inserted into the brachial artery, and the tTAC is obtained as dynamic PET images. However, serial arterial blood sampling is a burdensome procedure. Additionally, for the blood collector, there is a risk of radiation exposure, and for the patient, there is a risk of infection, bleeding, and thrombosis (Bedford and Wallman, 1973; Jons et al., 1997). Therefore, it is advantageous to omit serial arterial blood sampling without any loss of information for various functionalities obtained by quantitative analysis.

We have previously proposed a method for extracting the blood-related component based on independent component analysis (ICA): extraction of pTAC using ICA (EPICA) (Naganawa et al., 2003, 2005) from [^{18}F]fluorodeoxyglucose ([^{18}F]FDG) PET images. Dynamic PET images are assumed to be able to be decomposed into two independent source images: a blood volume image and a tissue image. The probability distributions of the voxel values in the two images are assumed to be statistically independent from each other. Most voxels include only brain tissues and a few voxels include blood vessels, therefore two images do not mostly overlap. Such a situation means spatially independent (McKeown et al., 1998). pTAC is extracted as a time course corresponding to the estimated independent image using spatial ICA. ICA decomposes dynamic PET images into a set of

* Corresponding author. Fax: +81 3 3964 2188.
E-mail address: ukimura@ieee.org (Y. Kimura).
Available online on ScienceDirect (www.sciencedirect.com).

1053-8119/$ - see front matter © 2005 Elsevier Inc. All rights reserved.
doi:10.1016/j.neuroimage.2005.02.025

images and a corresponding set of time–activity curves (TACs). Spatial ICA seeks mutually independent images. The EPICA procedures consist of appropriate preprocessing (difference-enhanced images) and spatial ICA using the cost function designed for extracting the pTAC to realize an effective pTAC extraction. We applied EPICA to dynamic [^{18}F]FDG PET images, and the estimated pTAC closely matched the measured pTAC.

In this paper, we investigated the applicability of EPICA to neuroreceptor imaging with Logan plots, as applied to dynamic [1-methyl-^{11}C]8-dicyclopropylmethyl-1-methyl-3-propylxanthine ([^{11}C]MPDX) PET images. [^{11}C]MPDX is a newly developed caffeine analogue tracer that has a high affinity for adenosine A_1 receptors (A1Rs), and it is a PET radioligand suitable for mapping A1Rs (Fukumitsu et al., 2003, 2005; Ishiwata et al., 2002). The Logan plot is applicable to analyzing the binding of [^{11}C]MPDX to A1Rs, and the cerebellum can be used as a reference region (Kimura et al., 2004). We propose a framework for estimating DVt and BP using Logan plots with the EPICA-estimated pTAC. The DVt images were generated by Logan plot using the EPICA-estimated pTAC and compared with those obtained by Logan plot using the measured pTAC. BP was calculated using a reference region based on the estimated DVt image and compared with that estimated using the nonlinear least squares method (NLSM).

Theory

The procedures of the proposed method, EPICA, are summarized and the framework for estimating DVt and BP without arterial blood sampling is proposed.

EPICA

The EPICA technique is briefly described here. More details are available in Naganawa et al. (2005). A measured TAC is assumed to be a linear combination of the activities originating within a tissue and within a plasma. Physiologically, the spatial distributions of the blood volume image and the tissue image are unrelated and statistically independent. A mathematical approach is applicable to decompose the measured PET images into two components. ICA is a statistical technique for decomposing observed data into statistically independent components (Bell and Sejnowski, 1995; Comon, 1994; Hyvärinen and Oja, 1997).

A measured TAC at the qth voxel is denoted as $\boldsymbol{x}(q) = [x_1(q), x_2(q), \ldots, x_F(q)]^T$, where $x_f(q)$ is the measured radioactivity at the fth frame. It is represented as a sum of TACs in a tissue and a plasma that are included in a single voxel. Therefore, the TAC at the qth voxel is described as:

$$\boldsymbol{x}(q) = s_p(q)\boldsymbol{c}_p + s_t(q)\boldsymbol{c}_t, \tag{1}$$

where $s_p(q)$ and $s_t(q)$ are the qth voxels of the blood volume image and the tissue image, respectively, and, $\boldsymbol{c}_p$ and $\boldsymbol{c}_t$ are column vectors that denote the pTAC and the tTAC, respectively. In matrix notation, Eq. (1) is described as:

$$\mathbf{X} = \boldsymbol{c}_p\boldsymbol{s}_p^T + \boldsymbol{c}_t\boldsymbol{s}_t^T = \mathbf{CS}, \tag{2}$$

where $\boldsymbol{s}_p$ and $\boldsymbol{s}_t$ are the blood volume image and the tissue image, respectively. The goal of ICA is to estimate the matrices $\mathbf{C}$ and $\mathbf{S}$ from the measured $\mathbf{X}$. The spatial distributions of tissues and blood vessels are anatomically distinguishable, and the ICA technique is expected to separate the blood-related component from the measured dynamic PET images. Note that there is an ambiguity in the amplitude of the estimated independent components because scale factors are canceled out between $\mathbf{C}$ and $\mathbf{S}$ (Comon, 1994).

Our proposed method, EPICA, is based on spatial ICA and adopts the FastICA algorithm (Hyvärinen, 1999; Hyvärinen and Oja, 1997). FastICA is a fast ICA algorithm based on fixed-point iterations and employs higher order statistics for estimating independent components. This algorithm has a remarkable performance such as fast convergence and robustness. The EPICA algorithm is summarized below. The EPICA procedure consists of three steps.

Step 1

Append the negative images $-\mathbf{X}$ to the measured PET images to realize the zero-mean data that are assumed by the ICA algorithm. The number of voxels becomes twice.

$$\mathbf{X}_N = [\mathbf{X}, -\mathbf{X}] \tag{3}$$

Step 2

Standardize each voxel's TAC using the time integral to emphasize the difference between the spatial distributions of tissues and blood vessels. Standardization is achieved by dividing each voxel's TAC by the time integral. The value of the standardized TAC at the fth frame is

$$x_{fE}(q) = \frac{x_f(q)}{\int_0^F x_f(q)\mathrm{d}f}. \tag{4}$$

Step 3

Perform FastICA using the proposed cost function.

In this step, a specially designed cost function is used that is sensitive to the difference between the spatial distributions of the tissues and blood vessels.

Formation of parametric images of DVt and BP

DVt at the qth voxel in a case of reversible binding is described as

$$\mathrm{DVt} = \frac{K_1(q)}{k_2(q)}\left(1 + \frac{k_3(q)}{k_4(q)}\right), \tag{5}$$

where $K_1(q)$, $k_2(q)$, $k_3(q)$, and $k_4(q)$ are kinetic parameters. The parameters $K_1(q)$ and $k_2(q)$ are rate constants of the transfer of radioligand between the plasma and free ligand compartments, and $k_3(q)$ and $k_4(q)$ are between the free ligand compartment and the specifically bound ligand compartments (Mintun et al., 1984). The Logan plot was used to compute DVt. Assuming that the brain blood volume is negligible, DVt is estimated using the following equation:

$$\frac{\int_0^T c_t(t)\mathrm{d}t}{c_t(T)} = \mathrm{DVt}\frac{\int_0^T c_p(t)\mathrm{d}t}{c_t(T)} + \mathrm{Const.}, \tag{6}$$

where $c_p(t)$ and $c_t(t)$ are the pTAC and the tTAC, respectively. Because there is an ambiguity in the amplitude of the estimated independent images and the corresponding TACs in EPICA, the derived DVt is a relative value.

If a receptor-free region (reference region) exists, BP ($=k_3/k_4$) can be calculated. Assuming that the distribution volume of the free/nonspecific region K_1/K_2 is constant across receptor-containing regions and a reference region, BP at the qth voxel is calculated as:

$$\mathrm{BP}(q) = \frac{k_3(q)}{k_4(q)} = \frac{\mathrm{DVt}(q)}{\mathrm{DVt'}} - 1, \tag{7}$$

where DVt' is the averaged DVt over a reference region. BP is the ratio of DVt in the receptor-containing region to DVt in the reference region. In a three-compartment model, the parameters that determine the scale of the tTAC are K_1 and the scale of the pTAC, while the other kinetic parameters (k_2, k_3, and k_4) determine the shape of the tTAC. In Eq. (7), the scale-related parameter K_1 is canceled out, which means that the scale of pTAC is not necessary in calculating BP. The reference region should be placed appropriately to obtain an accurate value of DVt'.

The cerebellum is assumed to be a valid receptor-free reference region for A1Rs (Fastbom et al., 1987; Kimura et al., 2004; Svenningsson et al., 1997), which can be defined manually. The roughly defined reference region probably includes voxels where specific bindings exist, and such voxels that have higher values of DVt should be excluded from the reference region. The threshold value is determined based on the estimated DVt image and the manually defined reference region is refined using the threshold value.

Materials and methods

[^{11}C]MPDX PET studies

The Ethics Committee of Tokyo Metropolitan Institute of Gerontology approved the study protocol. [^{11}C]MPDX PET studies were performed on 11 healthy volunteers and 14 patients (temporal lobe epilepsy, 7 patients; Alzheimer disease, 2; Parkinson disease, dementia, or dementia with Lewy bodies, 2; cerebrovascular disease, 1; brain tumor, 1; and mild cognitive impairment, 1), 19 males and 6 females with a mean age of 48.4 ± 23.5 years. Informed consent was given by all subjects. After a transmission scan with [^{68}Ga]/[^{68}Ge] rotating rod source for attenuation correction, [^{11}C]MPDX (589 ± 109 MBq) was injected intravenously and a dynamic PET scan was performed in two-dimensional mode using a Headtome-V (Shimadzu Co., Kyoto, Japan). Thirty slices, each with 128 × 128 voxels, were scanned over 40 min. The size of each voxel was 2 × 2 ×6.25 mm. The number of frames was 23 and the frame arrangements were 10 s × 6, 30 s × 3, 1 min × 5, 2.5 min × 5, and 5 min × 4. The arterial blood samples were taken via a catheter inserted in the brachial artery at 10, 20, 30, 40, 50, 60, 70, 80, 90, 100, 110, 120, 135, and 150 s, and 3, 5, 7, 10, 15, 20, 30, 40 min, and the plasma radioactivity was measured.

Formation of parametric images of DVt and BP

Images of DVt were formed by Logan plot with the EPICA-estimated pTAC and then BP images were derived with a reference region defined by the estimated DVt image. Extracranial voxels were manually excluded and 20 slices where subject's brain was located were used for the estimation of pTAC. The EPICA algorithm was implemented using MATLAB 6.5 (Mathworks Inc., MA, USA), and the code was executed on a 1.4-GHz Intel Pentium M computer, which was equipped with 768 MB of memory. DVt was estimated on a voxel-by-voxel basis by Logan plot. Slope estimates were made from the dynamic images from 10 to 40 min after injection (Kimura et al., 2004). A reference region was roughly drawn over the cerebellum. Voxels beyond the 80th percentile of DVt were excluded from the reference region. Parametric images of BP were generated according to Eq. (7) using the estimated DVt image and the refined reference region.

The DVt estimated using the EPICA-estimated pTAC was compared with that using the measured pTAC. ROIs were placed on the following regions: cerebellum; temporal, frontal, occipital, parietal, and medial frontal lobes; striatum; and thalamus; and the BPs of the parametric images were averaged over each ROI. For comparison, BPs in the ROIs were estimated using NLSM, where the distribution volume of the free/nonspecific region K_1/k_2 was estimated from cerebellum using a two-compartment model, and the kinetic parameters K_1, k_3, and k_4 of each ROI were estimated assuming that K_1/k_2 is constant across all ROIs. Note that this validation was performed about BP because our proposed framework provides only relative DVts and BPs.

Results

Estimation of the pTAC

A typical result for the estimated pTAC is shown in Fig. 1. Estimation of the pTAC by EPICA took approximately 10 s. Although the estimated pTAC deviated a little from the measured pTAC for the initial 3 min after the tracer injection, the overall shapes of the estimated and measured pTACs matched well. Typically, the ratio of the measured pTAC to a measured whole blood TAC kept 0.66 in the duration where Logan plot was applied.

Formation of parametric images of DVt and BP

Fig. 2 shows typical DVt images calculated using the EPICA-estimated pTAC and the measured pTAC, respectively, in a healthy

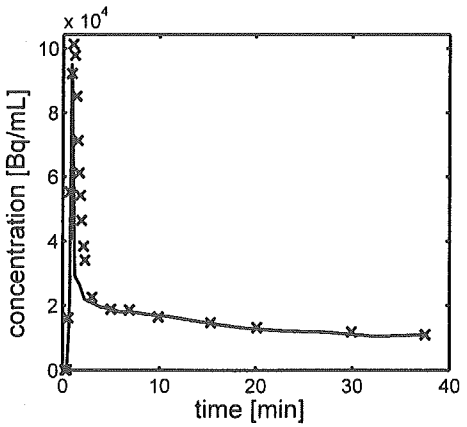

Fig. 1. Example of the EPICA-estimated pTAC (solid line) and the measured arterial blood samples (crosses). The scale of the EPICA-estimated pTAC was adjusted using the value at 37.5 min after [^{11}C]MPDX administration.